

PROBING PRE-PROTOSTELLAR CORES WITH FORMALDEHYDE

KAISA E. YOUNG, JEONG-EUN LEE, NEAL J. EVANS II

Department of Astronomy, The University of Texas at Austin, 1 University Station C1400, Austin, Texas 78712–0259

PAUL F. GOLDSMITH

Department of Astronomy, Cornell University, 522 Space Sciences Building, Ithaca, New York 14853

STEVEN D. DOTY

Department of Physics and Astronomy, Denison University, Granville, Ohio 43023

Draft version June 16, 2018

ABSTRACT

We present maps of the 6 cm and 1.3 mm transitions of H₂CO toward three cold, dense pre-protostellar cores: L1498, L1512, and L1544. The 6 cm transition is a unique probe of high density gas at low temperature. However, our models unequivocally indicate that H₂CO is depleted in the interiors of PPCs, and depletion significantly affects how H₂CO probes the earliest stages of star formation. Multi-stage, self-consistent models, including gas–dust energetics, of both H₂CO transitions are presented, and the implications of the results are discussed.

Subject headings: ISM: clouds, individual (L1498, L1512, L1544) — radio lines: ISM — stars: formation

1. INTRODUCTION

Molecular cloud cores that have yet to form a star provide the best opportunity to determine the initial conditions for star formation. However, the earliest evolution of a cloud core is very poorly constrained, and its evolutionary track is unclear. Recently, a number of compact objects without IRAS sources but with considerable submillimeter continuum emission have been identified (Ward-Thompson et al. 1994). Since these have no obvious source of internal luminosity but are characterized by high column density, they are plausible candidates for the stages just before formation of a central object. These objects are classified as Pre-Protostellar Cores, or PPCs.

Several of these objects have been mapped in submillimeter continuum emission (Shirley et al. 2000), and the dust emission has been modeled using self-consistent calculations of the dust temperature (Evans et al. 2001). The calculations show that the dust deep inside the PPCs is very cold ($T_d \sim 8$ K) and that this low T_d affects the interpretation of the submillimeter emission. In particular, the PPCs may be more centrally condensed, with higher central densities, than previously thought. Study of these objects will be very valuable for our understanding of the formation of solar-type stars. The density distribution as a function of radius in such starless cores is a strong discriminator between theoretical models. The density structure is also of critical importance for assessing whether the cloud is in equilibrium, or whether it may be beginning to collapse, and the density structure of PPCs strongly affects the nature of the collapse and star formation that follows (André et al. 2000).

Most density tracers employed by astronomers involve the use of a pair of rotational transitions of a linear molecule (e.g., isotopologues of CO, CS, HC₃N). Since the different transitions have different spontaneous decay rates, they require different collision rates to bring

their populations into thermal equilibrium. At a specific density, their relative populations reflect the collision rate and thus allow determination of the hydrogen density. This method can work well, but there is an important caveat: the different rotational levels generally lie at significantly different energies above the ground state, given approximately by the rigid-rotor formula $E(J) = hB_0J(J+1)$. For C¹⁸O, $J = 1$ is at 5.3 K, $J = 2$ is at 15.8 K, $J = 3$ at 31.6 K, etc. When we are dealing with a very cold cloud ($T \leq 10$ K) or a cloud whose temperature structure is unknown, a significant uncertainty is introduced. The collisional excitation rates, as well as the LTE level populations, for a linear molecule having a large rotation constant, including C¹⁸O, depend sensitively on the kinetic temperature of the gas. The lack of detailed temperature information means that the density one determines becomes confused with the temperature. It is extremely difficult to disentangle the two, especially in the case of cold dark clouds which may have warm edges heated by the interstellar radiation field. For PPCs, the heated edge can dominate the excitation effects and only with quite detailed models can we become confident that we have properly separated the temperature and the density structure.

Clearly a better probe of density for studying cold, dark clouds would be valuable. The lowest transition of ortho-formaldehyde (H₂CO) at 6 cm is one possible candidate. The 6 cm line is seen in absorption against the cosmic background radiation (CBR) in molecular clouds. The discovery of absorption against the cosmic background radiation by the lowest transition of H₂CO (Zuckerman et al. 1969) was quite surprising because it is impossible for any two-level system to have an excitation temperature below that of the CBR. The 6 cm transition occurs between the levels of the lowest K-doublet of H₂CO (the $J_{K_{-1}K_1} = 1_{11}$ and 1_{10} levels). Townes and Cheung (1969) proposed a collisional pumping scheme to

lower the excitation temperature; this scheme depends upon collisions to higher rotational levels followed by radiative decay to the $J = 1$ levels. The propensity of collisions to favor the lower levels in each excited K-doublet transition leads to an overpopulation of the lower level of the $J = 1$ K-doublet. This pumping scheme operates over a range of densities up to about 10^4 cm^{-3} , at which point collisions become dominant and drive the excitation temperature toward the kinetic temperature. Thus, there is a range of densities where $T_{ex} \sim T_{CBB}$ with no emission or absorption (Figure 1). At even higher densities, the line goes into emission. Because of trapping, the density above which the 6 cm line goes into emission depends on abundance. The 6 cm line could act as a unique tracer of cold, dense gas, because it does not require high temperatures to achieve significant fractional population of the upper level, but goes into emission *solely* as a result of high density.

The PPCs in this study are known to have high molecular hydrogen central densities ($n_c = 10^4 - 10^6 \text{ cm}^{-3}$; Evans et al. 2001) and, since there is no internal heat source, they should be very cold. Because the 6 cm transition goes from absorption to emission in these conditions (Figure 1), one might expect emission, weak absorption, or possibly neither toward the center of the PPCs. Vanden Bout, Snell, and Wilson (1983) observed deep 6 cm H_2CO absorption toward seven dark clouds. That study concluded that the 6 cm line was only probing the less dense outer envelope of the clouds.

Previous observations of the 6 cm H_2CO transition, including those of Vanden Bout et al. (1983), were carried out mostly with very large beams ($\sim 3'$ to $6'$), with the exception of a few observations with the VLA. In a VLA study of B335 (Zhou et al. 1990), a dark cloud in the early phases of forming a low mass star, the authors found a ring of absorption surrounding the center of the object. They proposed that the absence of absorption toward the center was caused by elevated densities near the center of the source. This proposal was verified by observations of the mm lines with the IRAM 30-m telescope, which in turn led to the identification of B335 as a collapsing protostar (Zhou et al. 1993). Additionally, the 6 cm line of H_2CO has been observed in emission toward regions of higher mass star formation, such as Orion (Zuckerman, Rickard, & Palmer 1975).

In this paper, we investigate this issue through high angular resolution observations of the 6 cm line in three PPCs. Sections 2 – 3 describe the observations and the results. Observations of an additional H_2CO transition at 1.3 mm are also described. In Section 4, we describe the methods used to model the line profiles and show how the observations can be explained by inclusion of depletion. These models are constrained by the additional modeling of the 1.3 mm H_2CO emission line observed toward the PPCs. Section 4.4 discusses the model results. A summary is provided in Section 5. A detailed discussion of the gas–dust energetics calculations is given in the Appendix.

2. OBSERVATIONS

Three PPCs, L1498 ($04^h10^m51.5^s$ $25^\circ09'58''$, J2000), L1512 ($05^h04^m08.2^s$ $32^\circ43'20''$), and L1544 ($05^h04^m17.1^s$ $25^\circ10'48''$), were observed in December 2001 and September 2002 using the 305-m telescope

of the Arecibo Observatory. All of the sources were observed at 6 cm, the $J_{K-1K_1} = 1_{11} - 1_{10}$ transition of ortho-formaldehyde. The observed frequency was 4829.6594 MHz, the weighted mean of the frequencies of the main hyperfine component ($F = 2 - 2$) and the nearby $F = 0 - 1$ component as given in Tucker, Tomasevich, & Thaddeus (1971). The Arecibo telescope has a beam size of $60''$ at this frequency. We observed at least 15 positions for each of three PPCs in the 6 cm line, creating maps with spectra spaced at $60''$ intervals. The mapping strategy ensured mapping off the edge of the core as seen in the dust. The long direction of each map is perpendicular to the long axis of the dust core. For L1544 and L1498, the long axis runs NW–SE; therefore, the map runs NE–SW.

The first challenge was to develop an appropriate data taking strategy. The standard Arecibo position switching routine, with off position designed to have the telescope observe the same “track” across the sky, is problematic, as these sources are large, and the reference position could “contaminate” the data. Switching to a fixed reference position was an option but would have had negative implications for data reduction. Fortunately, taking total power “ON SOURCE” spectra revealed that the receiver and autocorrelator (with digital bandpass filters) gave a baseline that was limited only by the fluctuations expected from the radiometer equation. This method also gains a factor of two in sensitivity compared to position switching, and should be of general value for observation of narrow spectral lines. As discussed in Section 3, this technique worked well for integration times as long as 200 min, resulting in rms fluctuations below 10 mK in a 1.5 kHz channel width.

Standard Arecibo calibration sources were observed at the beginning and end of each shift. In December 2001, the average beam efficiency, $\langle \eta_B \rangle$, including the main beam and the first sidelobe, from these observations was 0.61 ± 0.05 . In September 2002, $\langle \eta_B \rangle = 0.59 \pm 0.04$. This beam efficiency, η_B , accounts for radiation (ohmic) losses, rearward and forward scattering, and spillover. Assuming that the coupling efficiency is unity because of the extended nature of the dark clouds, we calculate the radiation (source) temperature, T_R , using the equation

$$T_R = T_A / \eta_B, \quad (1)$$

where T_A is the measured antenna temperature. T_R is outside the atmosphere. Table 1 lists the observed and derived 6 cm line properties, including T_R .

In addition to the 6 cm observations, each PPC was observed with the 10.4-m Caltech Submillimeter Observatory (CSO)¹ at 225.697787 GHz (1.3 mm), the frequency of the $J_{K-1K_1} = 3_{12} - 2_{11}$ transition of H_2CO . The CSO has a beamsize of $32''$ at 1.3 mm. The central position of L1544 was observed in October 1996. In January 2002 and September/October 2003, the central positions of L1498 and L1512 were observed, and five-point maps of all three PPCs were made. The four offset positions were along and perpendicular to the long axis of the core, all at $60''$ from the central position.

Observations of Mars and Jupiter as calibration sources gave an average main beam efficiency at 230 GHz

¹ The CSO is operated by the California Institute of Technology under funding from the National Science Foundation, contract AST 90-15755.

of $\langle\eta_{MB}\rangle=0.57\pm 0.11$ in October 1996, $\langle\eta_{MB}\rangle=0.53\pm 0.04$ in January 2002, and $\langle\eta_{MB}\rangle=0.77\pm 0.06$ in September/October 2003. Because the CSO employs a chopper wheel for calibration, the measured quantity is T_A^* , the antenna temperature corrected for atmospheric attenuation, radiation losses, and rearward spillover and scatter. Therefore, η_{MB} is η_B divided by η_{rss} , the ohmic and backward scattering efficiency. The radiation temperature in this case, again assuming the coupling efficiency is unity, is given by

$$T_R = T_A^*/\eta_{MB}. \quad (2)$$

All data were reduced using the Continuum Line Analysis Single-dish Software, CLASS. CLASS was used to remove baselines, average weighted spectra, and calibrate the data. The spectra were weighted by σ^{-2} , where σ is the rms noise. Spectra from different nights were averaged. The 6 cm data were then Hanning smoothed. The line center velocities (v_{LSR}), linewidths (Δv), and optical depths (τ) for the 6 cm data were determined by fitting a manifold of Gaussian profiles, one for each hyperfine component. Only one Gaussian component was necessary for the 1.3 mm data, because the hyperfine structure is negligible due to the extremely close spacing of the components.

3. RESULTS

Strong H_2CO 6 cm absorption was observed toward every source. The absorption spectra obtained at the central positions are shown in Figure 2. The radiation temperature and rms noise at each observed position is listed in Table 1 and fifteen-point maps of each PPC are shown in Figures 3 – 5. We achieved an average rms of 0.014 K at the center positions. At the other positions, the average rms was 0.022 K. The 6 cm line strength stayed nearly constant across all of the PPCs, not weakening until $120''$ from the central position.

We have achieved exceptionally good resolution of the hyperfine components of the 6 cm inversion doublet. The $F = 1 - 0$ hyperfine component ($\Delta\nu = -18.5$ kHz; Tucker, Tomasevich, & Thaddeus, 1971) was easily resolved in all of the PPCs. In L1498 and L1512, the $F = 1 - 2$ and $2 - 1$ hyperfine components ($\Delta\nu = +6.5$ and $+4.1$ kHz respectively) were also clearly distinguishable from the strong blend of the $F = 2 - 2$ and $F = 0 - 1$ components, which are closest to the observed central frequency of 4829.6594 MHz. In L1544, all of the components were blended except the $F = 1 - 0$ component creating an asymmetrical line profile.

The observed 6 cm linewidths are extremely narrow (~ 0.4 km s^{-1}), indicating low turbulent velocity dispersion. Table 1 lists the linewidth (Δv) and the turbulent velocity dispersion (σ_{turb}) for each source. To calculate the latter, we assumed $T_K = 10$ K. At the central positions, the H_2CO linewidths are comparable to those observed by Caselli et al. (2002a) in the N_2H^+ $J = 1 - 0$ line. However, they are about a factor of two smaller than those observed in the NH_3 (J, K) = (1, 1) inversion line by Benson and Myers (1989).

Table 1 also lists the excitation temperature for each position observed at 6 cm in the PPC maps. The excitation temperature was calculated using the optical depth and T_R (Heiles 1973). We assumed that there was only one velocity component and that the continuum temperature is 2.725 K (Mather et al. 1999). We find an average

excitation temperature of 1.5 K. This is consistent with the results of Heiles (1973), who found a mean excitation temperature of 1.6 K for 9 positions in dark dust clouds using a CBR temperature of 2.8 K. Vanden Bout et al. (1983) found a slightly higher mean excitation temperature of 1.9 K for 7 dark clouds.

A significant velocity gradient is seen across L1498. Overall, the velocity increases with distance away from the center position (Figure 6). This gradient is not consistent with either rotation or infall, but is suggestive of a cometary or prolate-shaped object seen face-on. A velocity gradient has been measured in C^{18}O (Lemme et al. 1995) and NH_3 (Goodman et al. 1993). However, the gradient runs SE–NW, along the main axis of the dust emission, which is very different from the H_2CO gradient. The apparent velocity gradient could be the result of two distinct velocity components, one associated with L1498 at 7.8 km s^{-1} and a second unrelated component at a higher velocity. Kuiper, Langer, & Velusamy (1996) observed a second component toward L1498 in C^{18}O and CS at 8.1 km s^{-1} . Tafalla et al. (2002) suggested that the second velocity component might be the result of gas unrelated to the dark cloud and equivalent to the “red” component in CS toward L1498 described by Lemme et al. (1995). The 6 cm H_2CO observations also show some evidence of a second velocity component in a small wing near 8.3 km s^{-1} (see also Section 4.1 below). Wang (1994) observed the 6 cm H_2CO line toward L1498 with a smaller beam at the VLA. Wang did not observe a velocity gradient, providing further evidence that the velocity gradient we observed is due to an unrelated second component.

The 1.3 mm observations toward the center of each PPC are shown in Figure 2. The 1.3 mm five-point maps are shown in Figure 3 – 5 along with the 6 cm absorption maps. The average rms for the 1.3 mm observations was 0.057 K. The 1.3 mm line was not detected at one offset position in each map. Two- σ upper limits for T_R are listed in Table 2 for positions with no detection along with T_R and rms at the other positions for each PPC. The upper limits given are small in comparison with the detected values, especially in L1512 and L1544. Therefore, the non-detections may indicate a real decrease of H_2CO emission in that direction (southeast in L1498, north in L1512, and southwest in L1544). Table 2 also lists v_{LSR} , Δv , and σ_{turb} for each position with a detection. The σ_{turb} agree with those found for the 6 cm lines within a channel width (± 0.06 km s^{-1} for the 1.3 mm data).

The H_2CO 6 cm maps indicate that the H_2CO absorption is considerably more extended than the dust continuum (Evans et al. 2001; Shirley et al. 2000). Vanden Bout et al. (1983) found that the 6 cm absorption extended over a region more than $10'$ in size toward L1544. However, the 1.3 mm emission, which only extends to $60''$, appears to drop off more quickly than the 6 cm H_2CO absorption in L1512 and L1544. Figure 7 shows normalized radial profiles of the H_2CO T_R for both 6 cm and 1.3 mm and the 850 μm emission along the short axis of the dark clouds. The broad extent of the 6 cm absorption and the smaller region of 1.3 mm H_2CO emission indicate that the two transitions are probing different parts of the PPCs. The 1.3 mm emission is likely tracing denser gas than the 6 cm absorption. This conclusion is discussed further in the context of our models

in Section 4.4 below.

4. MODELS

The H_2CO line profiles of each PPC were modeled in the final stage of a three step process. First, dust continuum data for the PPCs were modeled to determine the density and dust temperature profiles of each core. Second, the gas temperature structure was determined from the dust temperature with an energetics code. Finally, the density and gas temperature profiles were used to model the H_2CO lines using a Monte Carlo method code (Choi et al. 1995). The details of each stage are described below.

The observed sources have dust continuum maps at 450 and 850 μm (Shirley et al. 2000). The dust continuum radial intensity profile for L1498 was modeled by Y. Shirley et al. (in preparation), and L1512 and L1544 were modeled by Evans et al. (2001) yielding a density and dust temperature profile for each source. The temperature structure was modeled with a one-dimensional radiative transfer code (Egan, Leung & Spagna 1988). The density structure was assumed to be that of a Bonnor-Ebert sphere (Evans et al. 2001). The cloud was assumed to have no internal energy source and to be heated only by the interstellar radiation field (ISRF). A simulated observation of the cloud yielded a spectral energy distribution (SED) and a radial intensity profile. The model SED and radial profile were compared to the observations. The physical parameters of the model cloud were iteratively adjusted until a good fit was found to the observations. The best-fit model was judged by the reduced chi-squared of the model fit to the 450 and 850 μm radial profiles and the SED.

We remodeled L1512 and L1544 with a slightly different method than that used by Evans et al. (2001) but in accordance with Y. Shirley et al. (in preparation). Our models differed from the Evans et al. (2001) models in how the ISRF was treated. Evans et al. (2001) found that an ISRF reduced from the Black-Draine ISRF, which they adopted as a standard, improved the fit to the dust emission for L1512 and L1544. In the model for L1512, the ISRF (except for the CBR component) was multiplied by a factor of 0.3 and, in L1544, by a factor of 0.6. In the models presented here, the ISRF was instead attenuated to correspond to a certain visual extinction (A_V). The attenuated ISRF is reduced much more at ultraviolet and visible wavelengths but much less in the infrared than the ISRF reduced by a single multiplicative factor. Figure 8 plots both the reduced and attenuated ISRF for comparison.

The A_V values resulting from the dust models correspond well to the known environments of the PPCs. The best-fit dust model of L1498 required two magnitudes of visual extinction surrounding the core (Y. Shirley et al., in preparation). Cambr esy’s (1999) extinction map of Taurus shows L1498 to be fairly isolated and surrounded by ambient gas with $A_V = 1 - 2$ magnitudes. L1512 is on the edge of Taurus where A_V is about 0.5 magnitudes (Falgarone et al. 1998). For this PPC, attenuating the ISRF did not improve the fit to the dust, but since it was not a significantly worse fit, the $A_V = 0.5$ attenuated dust model was used for consistency. We found that attenuating the ISRF in the models for L1544 fit the dust emission radial profiles better than simply reducing

the ISRF. L1544 is the most heavily embedded core; our dust radiative transfer model indicates $A_V = 3$. This value is consistent with the extinction determined from star counts at a $5'$ radius ($A_V = 2 - 3$, Minn 1991; Snell 1981).

Once the dust temperature profile had been determined from the dust emission, an energetics code (after Doty & Neufeld 1997) was used to calculate the temperature of the gas from the temperature of the dust. The calculation accounted for radiative cooling of the gas, transfer of energy from collisions between the gas and dust grains, heating by cosmic rays, and photoelectric heating. The Appendix provides complete details of the energetics calculations.

The strength of the heating on the outside of the cloud in the energetics code is primarily controlled by the factor G_0 , which is the strength of the UV field relative to the standard ISRF at the outer PPC boundary. A value of G_0 less than unity results from the attenuation of the ISRF by the material surrounding the PPC, and a smaller G_0 indicates greater attenuation. In order to constrain the estimate of G_0 for each cloud, we modeled the CO $J = 1 - 0$ line and compared the models to observations for each PPC. This CO transition is completely thermalized. By comparing the strength of the modeled and observed CO lines, we are able to determine if the model temperature is too hot or cold on the outside of the cloud and, therefore, if G_0 is too high or low. We used the CO observations of Kuiper et al. (1996), Falgarone et al. (1998), and Tafalla et al. (1998) for L1498, L1512, and L1544 respectively. We did not attempt to fit the CO line profile in detail, because our models have many parameters other than G_0 . The CO models all had the same abundance and physical parameters. Different G_0 values were tested to find the one that produced a T_R that was consistent with the observations.

We compared G_0 found using CO observations as a constraint to G_0 calculated from the A_V value used to attenuate the ISRF in the dust model (see the equation for $G(r)$ in the Appendix) for each source. The CO-derived G_0 values were 0.06, 0.03, and 0.08 for L1498, L1512, and L1544. The G_0 values calculated from the dust model A_V were 0.03, 0.005, and 0.41, respectively. The G_0 values derived from CO are larger than those calculated from the A_V values for L1498 and L1544, indicating less extinction toward the PPCs. For L1512, the G_0 derived from CO is much smaller than the value calculated from the dust model A_V but is consistent with the G_0 values derived from CO for the other sources. Complete photon-dominated region (PDR) analysis is needed in order to fully examine this inconsistency. The CO-derived G_0 values are used in the energetics code for this work, because the CO is much more sensitive to G_0 than the dust models are to A_V . Further, the equation used to calculate G_0 for a given A_V is for plane-parallel slabs and is not appropriate for spheres as discussed in the Appendix.

We used the best fit density profile from the dust model and the gas temperature profile from the energetics calculations as input into a Monte Carlo (MC) method radiative transfer code (Choi et al. 1995) to model the H_2CO 6 cm and 1.3 mm lines. Figure 9 shows the density and temperature profiles resulting from the dust and energetics models for each PPC. The results from the MC code

were convolved to the resolution of the observations for comparison with the data. The MC model has two free parameters, the outer radius of the cloud (R_{out}) and the microturbulent velocity dispersion (δv_t). The same outer radius was used for the dust and MC models (0.15 pc) for consistency; δv_t was iterated on to find the best fitting value for each PPC. Theoretical collision rates for H_2CO only exist down to 10 K, and the temperatures in dark starless cores drop below that. Therefore, for the purpose of these models, the H_2CO collision rates were linearly extrapolated down to 3 K and 5 K from the known rates at 10 K and 15 K (Green 1991). The convergence criterion in the MC code was set at 5%. A more stringent convergence criterion of 2% was tested and did not significantly affect the model results.

The components of the hyperfine structure of the 6 cm line were modeled independently with the exception of the $F = 2 - 2$ and $F = 0 - 1$ components. These two components lie within 0.1 km s^{-1} of one another, less than the turbulent velocity dispersion in the observed lines. Therefore, the relative intensities of these lines were added together for the purpose of our models. The frequency of the combined component was given as the relative-intensity-weighted mean of the individual frequencies. The five modeled components were added for the complete modeled 6 cm line profile. We compared this method of modeling five components to modeling the full six hyperfine components and found that using all six components deepened the absorption by only about 10%.

Our models indicate that H_2CO is significantly depleted in these PPCs as predicted by various chemical models (Lee et al. 2004; Y. Aikawa 2003, private communication). Figure 10 shows the simulated 6 cm line profile for a dark cloud with a central density of 10^6 cm^{-3} and an undepleted H_2CO fractional abundance of 10^{-8} . The model is plotted with the observed line profile of L1544 to show the large discrepancy between the expected undepleted line profile and what was actually observed. The undepleted model predicts 6 cm *emission* toward the center of the PPC, a *qualitative* discrepancy with the observation. Depletion significantly affects how the 6 cm H_2CO transition probes cold, dense gas. If H_2CO is depleted in the center of a PPC, then the 6 cm line will not be able to see the densest part of the core.

Depletion was introduced into the models with an abundance profile characterized by less H_2CO at small radii than at larger radii. Several different functional forms of the abundance profile were compared in the modeling process, including a power law, exponential, and step function (see Table 6 in Lee et al. 2003). The abundance at the outer edge of the cloud was set by X_0 , the undepleted abundance. The shape of the step function and exponential were characterized by a radial scale of depletion (r_D). The depth of the step function was set by (f_D), the factor by which the abundance in the central portion of the PPC was decreased.

These simple functional forms of the abundance profile were also compared with the profile generated by chemical network models (Lee et al. 2004), where the reactions between gas and grains, such as depletion and desorption of species, as well as gas phase chemistry have been considered. Lee et al. (2004) used a series of Bonnor-Ebert spheres of various central densities (n_c) to calculate the evolution of chemistry in the PPC stage. They assumed

that a Bonnor-Ebert sphere evolves from lower central density to higher central density, and the timescale of the evolution decreases as the central density increases. The total timescale for the PPC stage was assumed to be a million years. The abundance profile resulting from the chemical models was multiplied by a scale factor ranging from 0.3 to 2.0 in the models to best fit the data since the actual timescale is unknown. Figure 11 shows examples of the various abundance profiles. The values specifying the exact shape of the abundance profiles (X_0 , r_D , f_D , n_c , etc.) were iterated on until a best fit for each type of profile was found for each source. The results of the models with different abundance profiles are compared below (Sections 4.1–4.4 and Table 3).

Each model was compared to the observed 6 cm line at the center of each PPC and at offsets of $60''$ and $120''$ from the center. The model was also compared to the 1.3 mm line at the center and $60''$ offset. Figures 12 – 14 plot the data and the best fitting model for each source. The offset spectra are the weighted average of the spectra in all directions at either $60''$ or $120''$ from the center of the cloud. For the 6 cm line, the $60''$ offset spectrum is the average of 8 spectra, and the $120''$ spectrum is the average of 6 spectra for each source. For the 1.3 mm line, the $60''$ offset spectrum is the average of 4 spectra.

The best model was selected by comparing values of the absolute deviation that characterize the model fit to the data at both wavelengths and all offsets. The absolute deviation is defined as the sum of $|\text{Model}(i) - \text{Observed}(i)|$ over all data points i (Press et al. 1992). The absolute deviation was chosen instead of the more common reduced chi-squared value in order to eliminate artificial weighting of the noisier 1.3 mm data. For nearly all the models, the 1.3 mm reduced chi-square was low compared to that for the 6 cm lines even when the model clearly fit the 6 cm data better than the 1.3 mm data. The high noise levels in the 1.3 mm data dramatically decreased the reduced chi-square values, and, as a result, created a bias toward the 1.3 mm fits. The absolute deviation does not consider noise so it is free of this bias.

We have calculated the absolute deviation in two different ways. First, we calculated the absolute deviation between the integrated intensity of the model and the observations. A second absolute deviation compares the line profile shape of the model and data. Each of these values is calculated for 6 cm and 1.3 mm lines independently. The absolute deviation is also calculated independently for each observed offset. The average absolute deviation over all offsets for each wavelength is reported in Table 3.

We chose the model with the lowest integrated intensity and profile absolute deviation values at 6 cm for the best-fit model because the 6 cm data have high signal-to-noise and provide good constraints for the models. All of the models presented in Table 3 are the best-fitting models for particular abundance profiles. There was often a discrepancy between the models with the lowest absolute deviation for the 6 cm data and the 1.3 mm data. We found that no reasonable models for the 6 cm data fit the 1.3 mm data well. This discrepancy is discussed in further detail in Section 4.4 below. The models are discussed by source in Sections 4.1 – 4.3.

4.1. L1498

L1498 is the most diffuse of the three PPCs discussed here. As a result, the best-fitting dust model has the lowest central density, 10^4 cm^{-3} , of all the sources (Figure 9). L1498 was modeled with an outer radius of 0.15 pc. This is smaller than the outer radius of the best-fitting dust radiative transfer model (0.17 pc, Y. Shirley et al., in preparation) but is consistent with the outer radii used by Lee et al. (2004) for the chemical models and for L1512 and L1544 in this work. All the L1498 models use $\delta v_t = 0.1 \text{ km s}^{-1}$. The G_0 derived from the CO observations of L1498 is 0.06. Table 3 gives a full listing of model parameters and absolute deviations for models of L1498 with differing abundance profiles.

The best-fitting model for L1498 (Figure 12) uses a chemical model abundance profile (Figure 11). The chemical model abundance profile was multiplied by a factor of 0.8 in order to best fit the data. The chemical model used had the same A_V as the dust model for L1498, $A_V = 2$, but a much higher central density of 10^7 cm^{-3} . The higher central density in the chemical model results in more central depletion of H_2CO in the abundance profile. Further, the chemical model abundance profile used to fit the L1498 data is dramatically different from the other abundance profiles at large radii (Figure 11). The chemical model abundance profile has a high maximum abundance ($\sim 9 \times 10^{-9}$) and decreases rapidly at large radii for $A_V = 2$. This abundance profile resulted in a model that fit the strength of the the 6 cm H_2CO absorption well at $60''$ and $120''$. The absorption predicted by the model at the center position appears too weak. The weak central line could indicate that there is not enough depletion at the center of the model, and the main hyperfine component is being driven toward emission. Alternatively, there could be less absorption in the main component because it is too optically thick in the model and is not probing as far into the cloud as the other components. Abundance profiles which have more central depletion but no outer decrease, fit the central 6 cm line better but were too deep at the offset positions.

An alternative model for L1498 was found by allowing G_0 to be a free parameter rather than constraining it with CO observations. An abundance profile, adopted from the chemical model with $A_V=2$ at the time step at which $n_c = 10^4 \text{ cm}^{-3}$ that is consistent with the model of the dust emission by Y. Shirley et al. (in preparation), can fit the observed 6 cm H_2CO profiles if a G_0 10 times higher than what was found from the CO $J = 1-0$ line is used. The absolute deviations for this model are listed in Table 3 along with the lower G_0 models. This model reproduces the 6 cm line profiles at all offsets well and does not have the same problem of weak center absorption as described above. In this chemical model, H_2CO is not very depleted even at the center because the depletion timescale is long at low density. This result shows that the strength of the ISRF (G_0) can greatly affect line profiles as discussed in Lee et al. (2004). Full PDR analysis and a better understanding of the environment is needed to correctly determine G_0 . Therefore, for the purposes of consistency in this paper, we have constrained G_0 by CO $J = 1-0$ observations with the caveat that the G_0 values derived may be underestimated.

The best-fitting model of L1498 illustrates a problem common in all our models. We did not adequately fit both the 6 cm data and the 1.3 mm data with the same

model parameters. The 1.3 mm models are consistently weaker than the observed emission lines when the 6 cm data is fitted well. For L1498, the best-fitting chemical model abundance profile did result in a better fit to the 1.3 mm data than the other abundance profiles modeled, although it was still too weak (Figure 12). The better fit to the 1.3 mm data may have resulted from the fact that the chemical model abundance profile has a higher maximum abundance than the other profiles, although it drops off to comparatively much lower abundances at large radii (Figure 11). In general, the 1.3 mm data could be fit with a larger X_0 , which results in too much absorption at 6 cm. The difficulty in fitting both the 6 cm and 1.3 mm data with one model is discussed further in Section 4.4 below.

The model also does not fit the data well to the right of the main 6 cm H_2CO hyperfine component in L1498. The data show a wing around 8.3 km s^{-1} that the models do not reproduce. We postulate that this wing is due to a second velocity component caused by unrelated gas. A second velocity component has also been observed in C^{18}O and CS (Kuiper et al. 1996) as described above in Section 3.

4.2. L1512

L1512 is best fitted with a model of a moderate central density ($n_c = 10^5 \text{ cm}^{-3}$) and a step function abundance profile. All the L1512 models had an outer radius of 0.15 pc, a δv_t of 0.1 km s^{-1} , and $G_0 = 0.03$. Model parameters and results are given in Table 3 and Figures 9 and 13. As Figure 13 shows, the step function model predicts less 6 cm absorption in the main hyperfine component ($F = 2-2$) than observed at the center of L1512. The other abundance profiles modeled predict even less absorption than the step function model. The step function abundance profile differs significantly from the power law, exponential, and chemical model profiles in that H_2CO is depleted out to a larger radius. The other profiles fall off gradually, but the step function has a steep drop in abundance at 0.05 pc. Although the best-fit model is not a perfect match to the data, the model constrains the H_2CO abundance profile by ruling out profiles that are depleted too slowly toward the center of the core. The parameters characterizing the best-fit step function (r_D , f_D , X_0) are good within a factor of two to fit the data.

Again, the best-fit model produces 1.3 mm line profiles that are too weak compared to the data (see Section 4.4 below). Additionally, there is a velocity shift between the model and 1.3 mm data at the $60''$ offset position. The central velocity of the data appears higher than that of the model. The map of L1512 in Figure 4 shows that there is no obvious velocity gradient in the 6 cm data as is the case in L1498.

As with L1498, the models do not fit the wing to the right of the main 6 cm hyperfine component as shown in Figure 13, and we believe that this again is the result of a second velocity component. Falgarone et al. (1998) observed multiple velocity components in several transitions of CO toward L1512. They observed a second velocity component in the line profile of C^{18}O at a similar velocity ($7.3 - 8.1 \text{ km s}^{-1}$) to the wing in the H_2CO line.

4.3. L1544

L1544 is the most centrally condensed of the three PPCs. The models require a high central density ($n_c = 10^6 \text{ cm}^{-3}$; Figure 9) and a larger G_0 of 0.08 compared to the other PPCs. All the L1544 models have an outer radius of 0.15 pc and δv_t of 0.19 km s^{-1} . There was no clear best-fitting model for L1544. The absolute deviation values were very similar for models with four different abundance profiles. The model parameters and absolute deviations are shown in Table 3. Even though the exact shape of the abundance profile for L1544 cannot be determined by these models, the general shape of the abundance profile is constrained. All of the best-fitting abundance profiles have a similar shape at large radii, are depleted toward the center on a radial scale (r_D) of 0.03 to 0.04 pc, and have a outer edge undepleted H_2CO fractional abundance (X_0) of about 2×10^{-8} (Figure 11). Changes in r_D and X_0 of 25% produce significantly different model results and absolute deviations, showing that the reported values characterize the general shape of the H_2CO abundance profile. Figure 14 shows the model fit to the data for a power law abundance profile. The power law models have slightly lower absolute deviations for the 6 cm data than the models with different abundance profiles.

In the L1544 models, the model 1.3 mm line at the center position shows self-absorption (Figure 14). Self-absorption is not seen in our observations, although the spectra are noisy. We have tried to reconcile our models and the data in two ways. First, the density at large radii representing the ambient density of a molecular cloud was increased from 1000 cm^{-3} to 3000 cm^{-3} . The modeled 1.3 mm lines were stronger but still showed deep self-absorption in the models with larger outer density. L1544 is thought to be undergoing infall (Tafalla et al. 1998; Caselli et al. 2002b), and we have incorporated an infall velocity into the model. Two different velocity profiles were used, an ambipolar diffusion model from Ciolek & Basu (2000, time t_3 in Figure 2) and a Plummer-like model (Whitworth & Ward-Thompson 2001; Lee et al. 2003 (Fig. 4)). The absolute deviation values for a model with a power law abundance profile and a Plummer-like velocity profile are listed in Table 3. For both types of velocity profiles, the effects on the model results were small for the 6 cm lines. The 1.3 mm modeled lines still retained the self-absorption feature. However, the 1.3 mm lines were also asymmetrical, skewed to the blue, at both offsets (Figure 14). This effect was more pronounced with the Ciolek & Basu (2000) velocity profile. The noise makes the determination of an asymmetrical profile difficult in the 1.3 mm data for L1544. A skewed 1.3 mm line profile cannot be ruled out.

4.4. Discussion

An unambiguous aspect of our models is that all require depletion of formaldehyde in the center of the core. Depletion of carbon-bearing molecules such as CO and CS in the center of PPCs, including L1498, L1512 and L1544, is well known (e.g., Tafalla et al. 2004; Lee et al. 2003, Tafalla et al. 2002). Tafalla et al. (2004) modeled high angular resolution C^{18}O and CS observations toward L1498 with a similar method to the one in this work, except that they assumed a constant dust temper-

ature and used a larger outer radius (0.25 pc). They found the high resolution data required a faster decrease in abundance than their previous models of lower resolution data had suggested (Tafalla et al. 2002). Their result is consistent with the findings presented here that, although the exact shape of the abundance profile cannot be uniquely determined, all the models suggest a significant drop in abundance toward the center of PPCs. Tafalla et al. (2004) fit the CO and CS data with a step function abundance profile that drops to zero at a given radius. They found depletion radii about a factor of two larger for CO and CS than the depletion radius used in the step function abundance profile model of H_2CO in L1498 (Table 3). Lee et al. (2003) also found C^{18}O to be depleted out to larger radii ($r_D = 0.075$ and 0.045 pc) and by a larger factor ($f_D=25$) in L1512 and L1544 than is required for H_2CO in the models presented here.

The depletion of H_2CO in PPCs may be related to the chemical processes of deuteration and the reaction between gas and grains. H_2CO is likely depleted in PPCs due to accretion onto cold dust grains (Carey et al. 1998). Maret et al. (2004) observed a jump in the abundance of gas-phase H_2CO where grain mantles evaporate ($T_D = 100$ K) in Class 0 protostellar envelopes, supporting the idea of depletion onto grains. In addition, at high density and very low temperature, D_2CO forms efficiently (Tielens 1983) because of its lower zero energy level compared to that of H_2CO . D_2CO is considered to form both through gas chemistry and surface chemistry (Ceccarelli et al. 2002). In dark cores without protostellar objects, abundant deuterated molecules in the gas phase are mainly driven by gas chemistry because the dust temperature is not high enough for deuterated molecules on grain surfaces to be desorbed. Gas-phase deuteration may be more efficient where CO and NH_3 are depleted, as in PPCs (Roberts & Millar 2000; Bacmann et al. 2003). D_2CO , which is formed and accumulated on grain surfaces during the PPC stage, evaporates when a newly formed luminous source heats dust grains (Loinard et al. 2002).

In addition to depletion, another aspect of the model results warrants further discussion. No single model was able to fit the 6 cm and 1.3 mm data simultaneously. We have considered different explanations for this discrepancy. First, we have tried four different abundance profiles: step function, power law, exponential, and chemical model. Table 3 lists the model parameters for each type of abundance profile and the corresponding absolute deviations. The table shows that there is not one clear best-fitting model abundance profile for all of the sources. The power law, exponential, and chemical model abundance profiles are all very similar (Figure 11) and often result in comparable line profiles. None of the abundance profiles solves the problem of fitting the data at both wavelengths. For those models providing a good match to the 6 cm observations, the models consistently underpredict the 1.3 mm line strength in L1498 and L1512 and show 1.3 mm self-absorption in L1544.

Second, we increased the collision rates for the transitions that populate the upper level of the 1.3 mm transition by a factor of three. This change did increase the model 1.3 mm emission by a factor of 1.75 on average. However, the transitions to the upper level of the 1.3 mm transition are also significant in the pumping mechanism

that allows for 6 cm absorption against the CBR. The increase in collision rates increased the efficiency of cooling of the 6 cm absorption, and the absorption in the models deepened by more than a factor of 2. Therefore, a model with increased collision rates did not fit the 6 cm and 1.3 mm observed line profiles simultaneously.

Since changing the abundance profiles and collision rates did not solve the discrepancy between the 6 cm and 1.3 mm line models, we suggest that a density profile other than the Bonner-Ebert sphere may be needed to simulate the observed 6 cm and 1.3 mm data. The two transitions are most sensitive to only slightly different densities in emission, but the 6 cm absorption can come from a region of significantly lower density (Figure 1). The strong 6 cm absorption could mask weak 6 cm emission coming from the denser regions. Therefore, we are, in effect, seeing two different parts of the cloud with the two transitions, and a more complex density profile may be able to match both lines. The Bonner-Ebert density profile has been found to fit submillimeter dust continuum data well in PPCs (Evans et al. 2001). Deviations from spherical symmetry in the PPCs not accounted for in the models may be contributing to the discrepancy in the 6 cm and 1.3 mm models. However, a three-dimensional radiative transfer model of the dust continuum emission from L1544 fits a power-law density profile to the data and cannot rule out a Bonner-Ebert density profile similar to that of the best fit one-dimensional model (S. Doty et al., in preparation). The strength of the 1.3 mm lines at both $0''$ and $60''$ suggests that there is more dense material further out in the cloud than the Bonner-Ebert or power law density profiles allow. One solution may be to include small regions of enhanced density in the models. High-density clumps would not be resolved in the dust continuum and may not be large enough to affect the strength of the 6 cm line but could provide enough dense material in the outer parts of the cloud to produce the observed 1.3 mm H_2CO lines. Additionally, the temperature and density dependences are not as well decoupled in the 1.3 mm transition as in the 6 cm transition. Small regions of higher temperature may also create the excess 1.3 mm emission observed.

5. SUMMARY

We have presented maps of three PPCs in two transitions (6 cm and 1.3 mm) of formaldehyde showing strong absorption in the 6 cm transition toward all the sources. The absorption extended well beyond the edge of the observed dust emission. The 1.3 mm emission was observed out to $60''$ in all the PPCs. A velocity gradient, increasing away from the center of the core, was observed in L1498. The apparent gradient may be caused by unrelated gas in the region of L1498.

We have modeled both H_2CO transitions, including the offset positions, with a multi-stage method including dust radiative transfer, gas energetics, and gas radiative transfer. The attenuation of the ISRF, reflected in the parameter G_0 in the energetics code, was constrained by CO observations. However, since G_0 can have a significant effect on the model results, full PDR analysis is needed to better constrain this parameter and future PPC models.

The models described in this work indicate that H_2CO is depleted in the center of these PPCs as predicted by chemical network models. Undepleted models cannot reproduce the strong 6 cm absorption but predict 6 cm emission toward the center of the cold, dense PPCs. Therefore, the 6 cm H_2CO transition is not able to probe the densest parts of PPCs. Although all the models require depletion of H_2CO , the shape of the abundance profile in the best-fitting models varies from source to source. L1498 is fitted best with a chemical model abundance profile that is depleted both toward the center and at large radii. L1512 requires a large amount of depletion out to a relatively large radius, so is fitted with a step function abundance profile. L1544 is fitted best with a power law abundance profile that depletes smoothly toward the center. The models place strong constraints on the physical parameters of the core at large radii and unequivocally indicate depletion of H_2CO toward the center of PPCs.

The models also show that multiple velocity components may be present in the 6 cm H_2CO observations of L1498 and L1512. The 1.3 mm and the 6 cm data cannot be well matched with a single model. Models that are reasonable fits to the 6 cm data are unable to reproduce the strength of the 1.3 mm emission. The 1.3 mm emission may be probing denser gas than the 6 cm absorption. A more complex density or temperature distribution may be needed to fit both sets of data.

6. ACKNOWLEDGMENTS

We are grateful to H. Hernandez, K. Allers, J. Wu, A. Bauer, and M. Enoch for their long nights at Arecibo and the CSO helping to obtain the data for this paper. This material is based in part on work supported by the National Aeronautics and Space Administration under Grant No. NGT5-50401 issued through the Office of Space Science (KEY). This work was also supported by grants AST-9988230 and AST-030725 from the National Science Foundation (NJE) and by a grant from the Research Corporation (SDD). The National Astronomy and Ionosphere Center is operated by Cornell University under a Cooperative Agreement with the National Science Foundation.

REFERENCES

- André, P., Ward-Thompson, D., & Barsony, M. 2000 in *Protostars and Planets IV*, ed. V. Mannings, A. Boss, S. Russell (Tucson: Univ. Arizona), 59
- Bacmann, A., Lefloch, B., Ceccarelli, C., Steinacker, J., Castets, & Loinard, L. 2003, *ApJ*, 2003, 585, L55
- Bakes, E. L. O., & Tielens, A. G. G. M. 1994, *ApJ*, 427, 822
- Benson, P. J., & Myers, P. C. 1989, *ApJS*, 71, 89
- Burke, J. R., & Hollenbach, D. J. 1983, *ApJ*, 265, 223
- Cambrésy, L. 1999, *A&A*, 345, 965
- Carey, S. J., Clark, F. O., Egan, M. P., Price, S. D., Shipman, R. F., & Kuchar, T. A. 1998, *ApJ*, 508, 721
- Caselli, P., Benson, P. J., Myers, P. C., & Tafalla, M. 2002a, *ApJ*, 572, 238
- Caselli, P., Walmsley, C. M., Zucconi, A., Tafalla, M., Dore, L. & Myers, P. C. 2002b, *ApJ*, 565, 331
- Ceccarelli, C., Vastel, C., Tielens, A.G.G.M., Castets, A., Boogert, A.C.A., Loinard, L., & Caux, E. 2002, *A&A*, 381, L17
- Choi, M., Evans, N. J., II, Gregersen, E. M., & Wang, Y. 1995, *ApJ*, 448, 742
- Ciolek, G. E. & Basu, S. 2000, *ApJ*, 529, 925
- Doty, S. D. & Neufeld, D. A. 1997, *ApJ*, 489, 122

- Doty, S. D., van Dishoeck, E. F., van der Tak, F. F. S., & Boonman, A. M. S. 2002, *A&A*, 389, 446
- Egan, M. P., Leung, C. M., & Spagna, G. R., 1988, *Comput. Phys. Comm.*, 48, 857
- Evans, N. J., II, Rawlings, J. M. C., Shirley, Y. L., & Mundy, L. G. 2001, *ApJ*, 557, 193
- Falgarone, E., Panis, J.-F., Heithausen, A., Pérault, M., Stutzki, J., Puget, J.-L., & Bensch, F. 1998, *A&A*, 331, 669
- Flannery, B. P., Roberge, W., & Rybicki, G. B. 1980, *ApJ*, 236, 598
- Goldsmith, P. 2001, *ApJ*, 557, 736
- Goodman, A. A., Benson, P. J., Fuller, G. A., & Myers, P. C. 1993, *ApJ*, 406, 528
- Green, S. 1991, *ApJS*, 76, 979
- Heiles, C. 1973, *ApJ*, 183, 441
- Hollenbach, D. & McKee, C. F. 1989, *ApJ*, 342, 306
- Hollenbach, D. J., Werner, M. W., & Salpeter, E. E. 1971, *ApJ*, 163, 165
- Juvela, M., Padoan, P., & Jimenez, R. 2003, *ApJ*, 591, 258
- Kuiper, T. B. H., Langer, W. D., & Velusamy, T. 1996, *ApJ*, 468, 761
- Lee, J.-E., Evans, N. J., II, Shirley, Y. L., & Tatematsu, K. 2003, *ApJ*, 583, 789
- Lee, J.-E., Bergin, E. A., & Evans, N. J., II 2004, *ApJ*, submitted
- Lemme, C., Walmsley, C. M., Wilson, T. L., & Muders, D. 1995, *A&A*, 302, 509
- Loinard, L., et al. 2002, *P&SS*, 50, 1205
- Maret, S. et al. 2004, *A&A*, 416, 577
- Mather, J. C., Fixsen, D. J., Shafer, R. A., Mosier, C., & Wilkinson, D. T. 1999, *ApJ*, 512, 511
- Mathis, J. S., Ruml, W., & Nordsieck, K. H. 1977, *ApJ*, 217, 425
- Minn, Y. K. 1991, *J. Korean Astron. Soc.*, 24, 191
- Neufeld, D. A., & Kaufman, M. J. 1993, *ApJ*, 418, 263
- Neufeld, D. A., Lepp, S., & Melnick, G. J. 1995, *ApJS*, 100, 132
- Ossenkopf, V. & Henning, Th. 1994, *A&A*, 291, 943
- Press, W. H., Teukolsky, S. A., Vetterling, W. T., & Flannery, B. P. 1992, *Numerical Recipes in FORTRAN* (2d ed; Cambridge: Cambridge Univ. Press)
- Roberts, H. & Millar, T. J. 2000, *A&A*, 364, 780
- Shirley, Y. L., Evans, N. J., II, Rawlings, J. M. C., & Gregersen, E. M. 2000, *ApJS*, 131, 249
- Snell, R. L. 1981, *ApJS*, 45, 121
- Tafalla, M., Mardones, D., Myers, P. C., Caselli, P., Bachiller, R., Benson, P. J. 1998, *ApJ*, 504, 900
- Tafalla, M., Myers, P. C., Caselli, P., & Walmsley, C. M. 2004, *A&A*, 416, 191
- Tafalla, M., Myers, P. C., Caselli, P., Walmsley, C. M., & Comito, C. 2002, *ApJ*, 569, 815
- Tielens, A. G. G. M. 1983, *A&A*, 119, 177
- Townes, C. H. & Cheung, A. C. 1969, *ApJ*, 157, L103
- Tucker, K. D., Tomasevich, G. R., & Thaddeus, P. 1971, *ApJ*, 169, 429
- Vanden Bout, P. A., Snell, R. L., & Wilson, T. L. 1983, *A&A*, 118, 337
- van der Tak, F. F. S. & van Dishoeck, E. F. 2000, *A&A*, 358, L79
- Wang, Y. 1994, Ph.D. Thesis, The University of Texas at Austin
- Ward-Thompson, D., Scott, P. F., Hills, R. E., André, P. 1994, *MNRAS*, 268, 276
- Whitworth, A. P., Ward-Thompson, D. 2001, *ApJ*, 547, 317
- Zhou, S., Evans, N. J., II, Butner, H. M., Kutner, M. L., Leung, C. M., & Mundy, L. G. 1990, *ApJ*, 363, 168
- Zhou, S., Evans, N. J., II, Kömpe, C., & Walmsley, C. M. 1993, *ApJ*, 404, 232
- Zuckerman, B., Palmer, P., Snyder, L. E., Buhl, D. 1969, *ApJ*, 157, L167
- Zuckerman, B., Rickard, L. J., & Palmer, P. 1975, *ApJ*, 197, 571

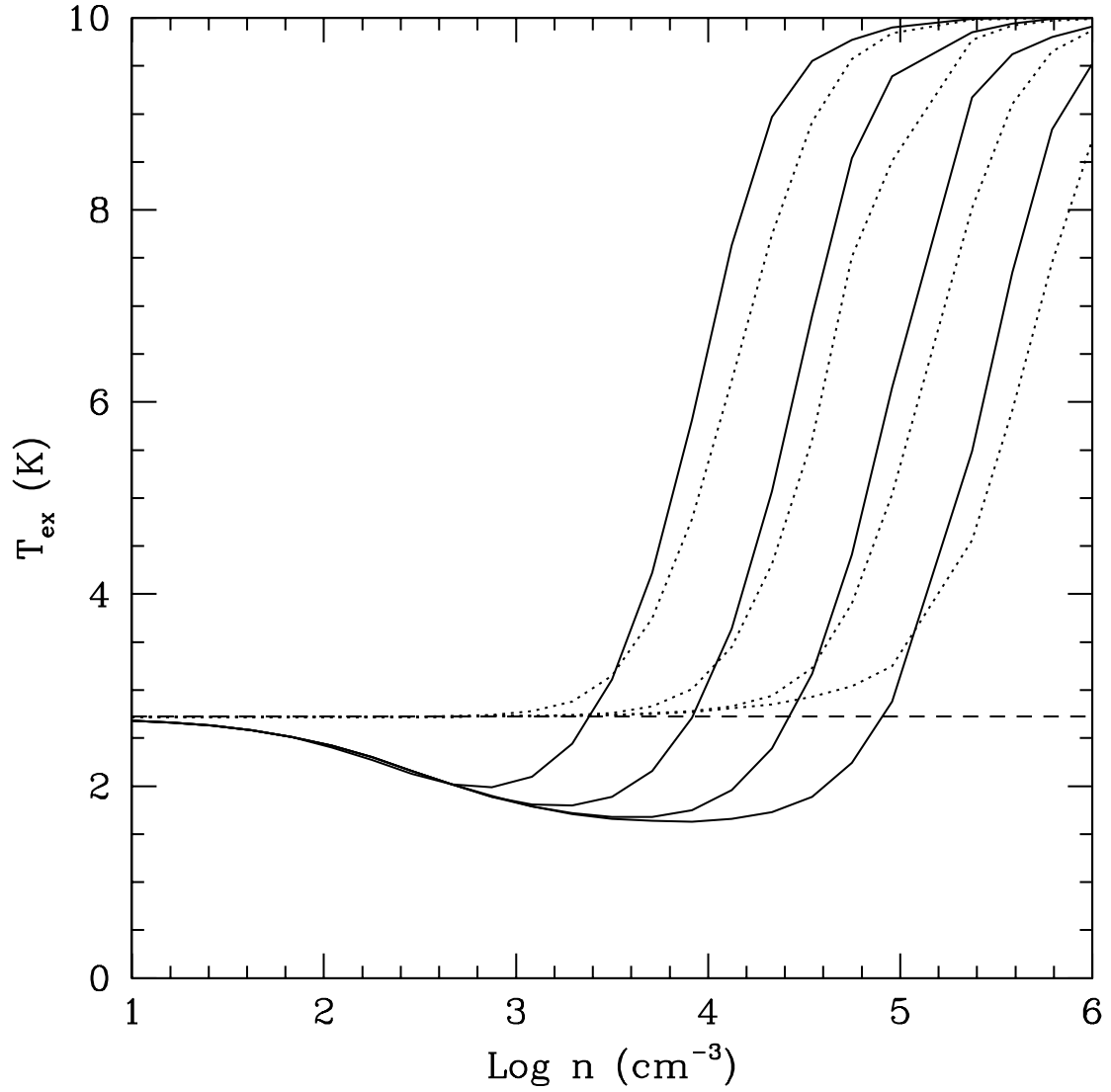


FIG. 1.— Plot of the excitation temperature of the H₂CO 6 cm (solid lines) and 1.3 mm (dotted lines) transitions at different abundances versus the log of the molecular hydrogen density. The H₂CO fractional abundance decreases from left to right for the curves in the plot, $X = 10^{-7}, 10^{-8}, 10^{-9}, 10^{-10}$. The dashed line is the temperature of the CBR (2.725 K). The plot was generated assuming $T_K = 10$ K, using an LVG code with $dv/dr = 1 \text{ km s}^{-1} \text{ pc}^{-1}$.

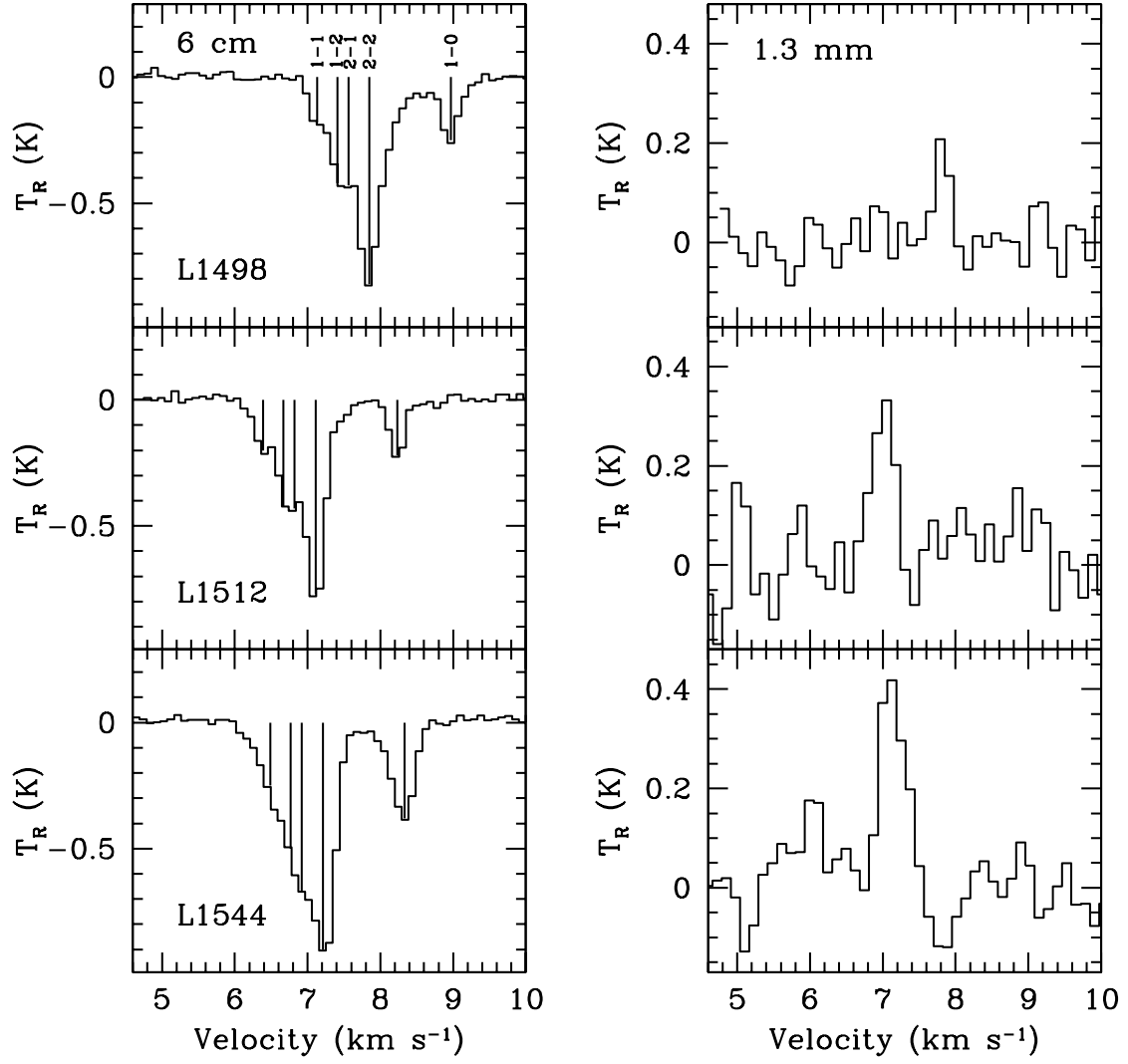


FIG. 2.— Spectra of H_2CO in the dark clouds L1498, L1512, and L1544. Panels in the left column show the 6 cm absorption against the CBR. The 6 cm hyperfine components are marked with vertical lines and labeled in the top panel. The $F = 0 - 1$ component is not marked, because it is blended with the strongest component, $F = 2 - 2$. Panels in the right column show the 1.3 mm emission toward the centers of the PPCs.

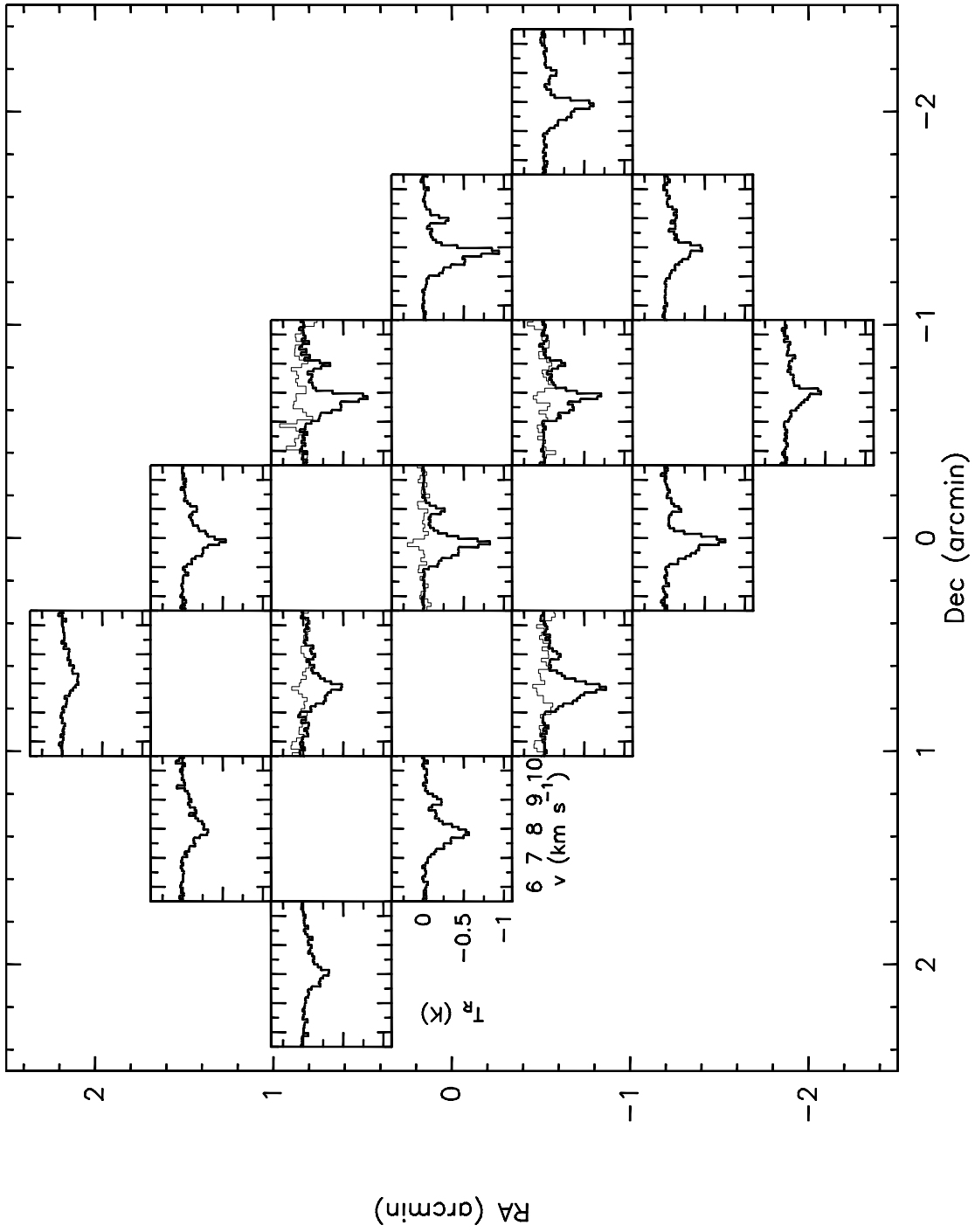


FIG. 3.— Map of H₂CO 6 cm absorption (thick lines) and 1.3 mm emission (thin lines) in L1498.

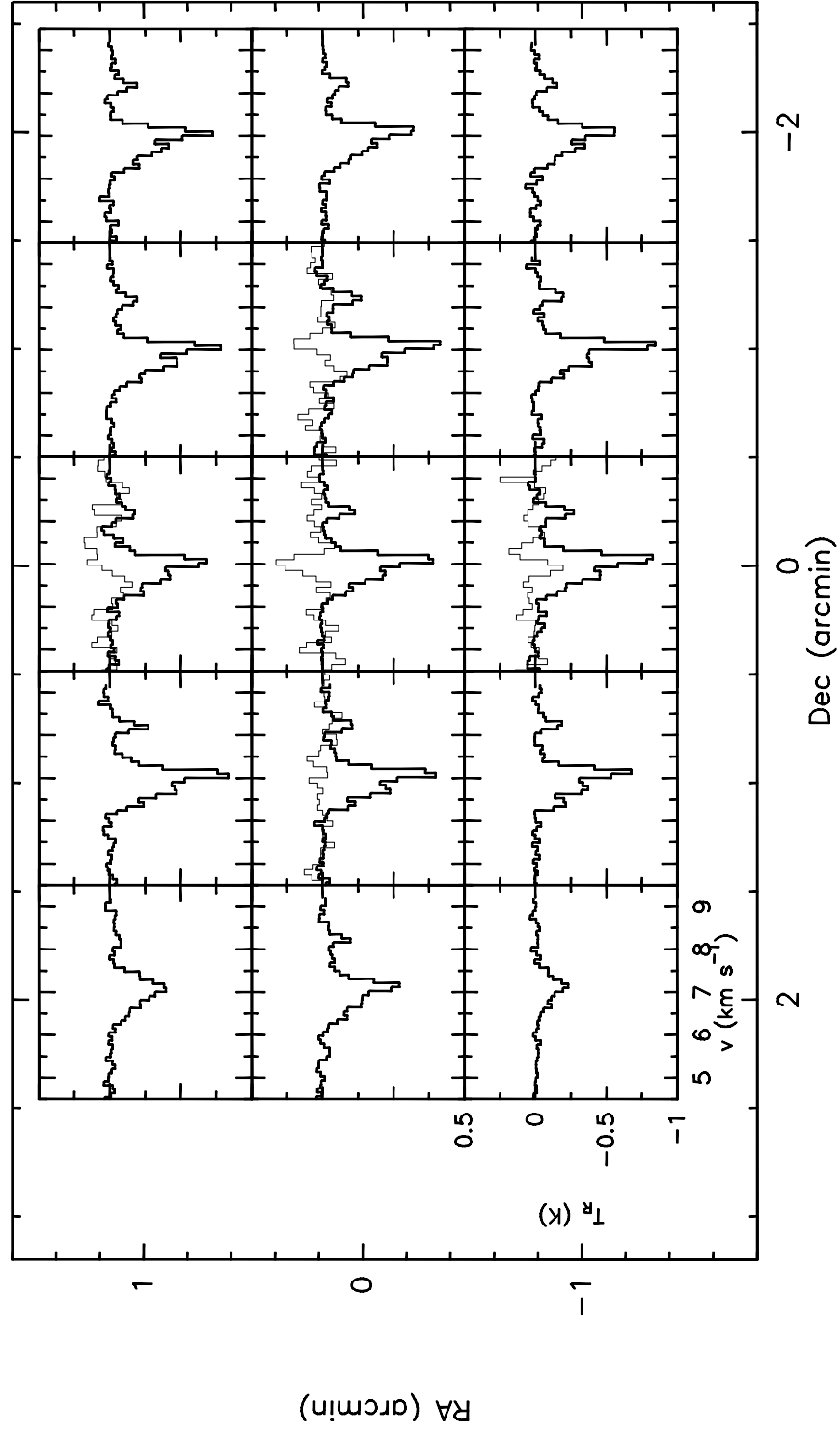


FIG. 4.— Map of H_2CO 6 cm absorption (thick lines) and 1.3 mm emission (thin lines) in L1512.

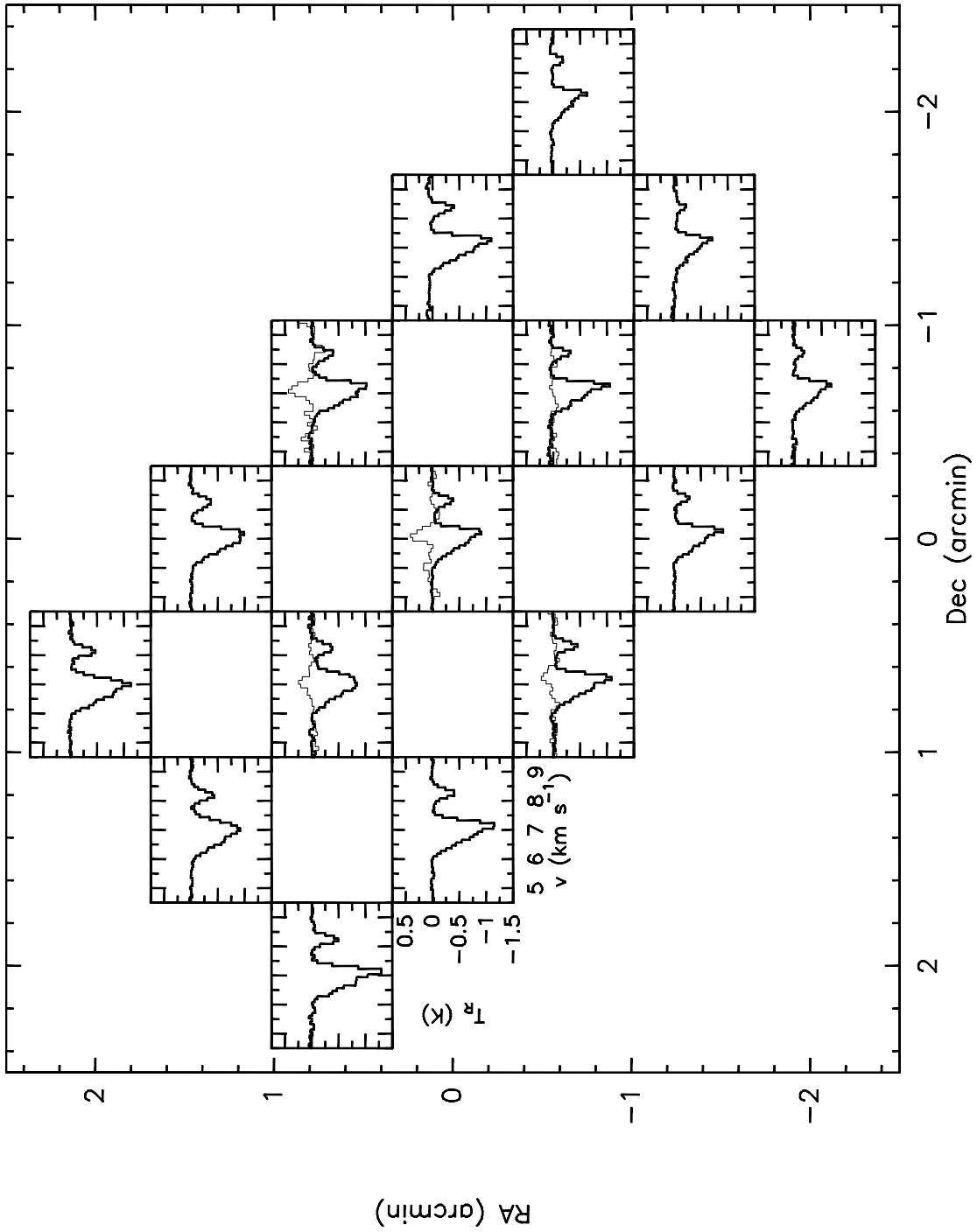


FIG. 5.— Map of H₂CO 6 cm absorption (thick lines) and 1.3 mm emission (thin lines) in L1544.

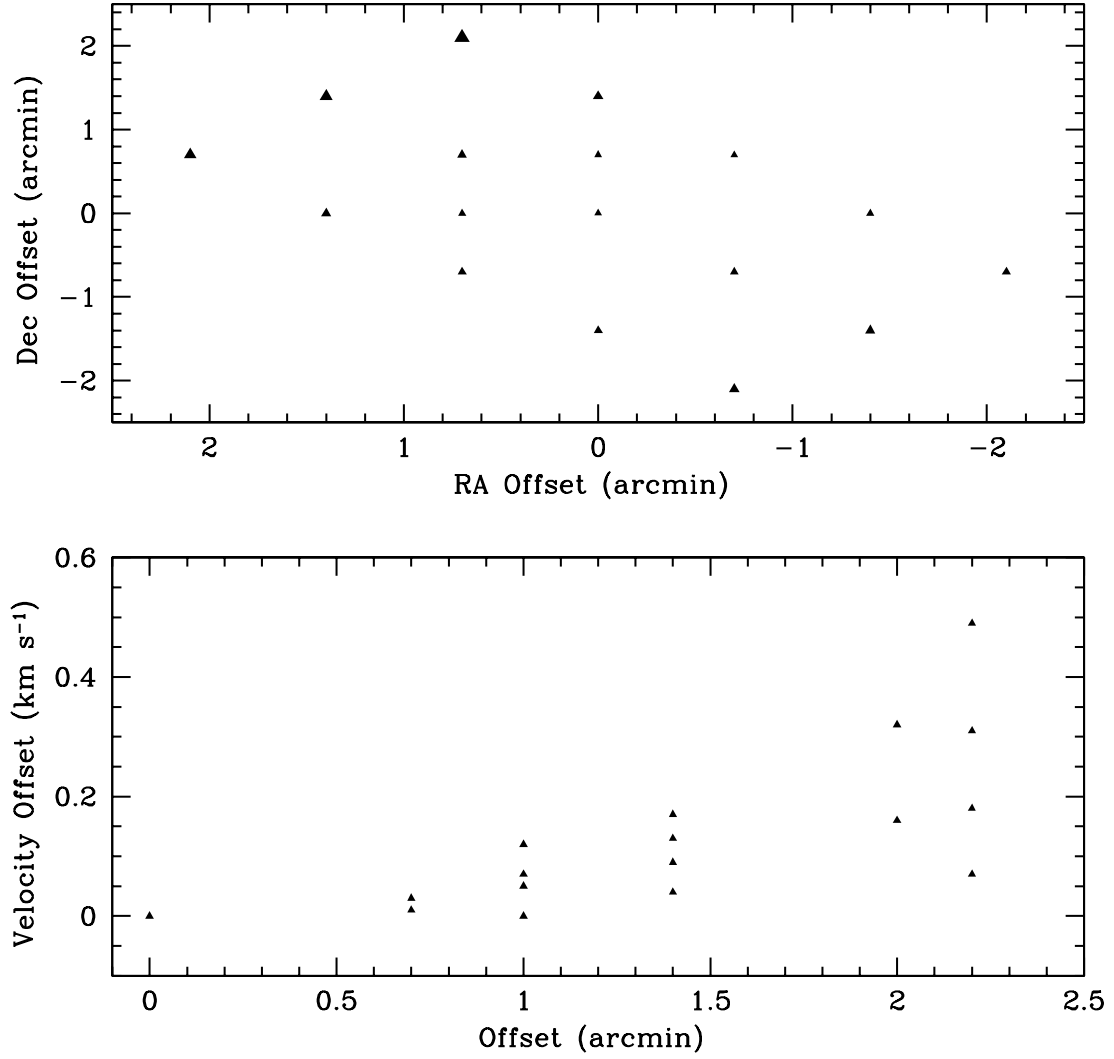


FIG. 6.— The top panel shows the velocity gradient in the 6 cm line in L1498 in RA–Dec space. The size of the symbol increases with velocity. The central (and smallest) velocity is 7.85 km s^{-1} and the largest velocity is 8.34 km s^{-1} . All velocities are listed in Table 1. The bottom panel shows the velocity difference versus the positional offset. This plot shows that the velocity, as well as the dispersion of velocities, increases with distance from the center.

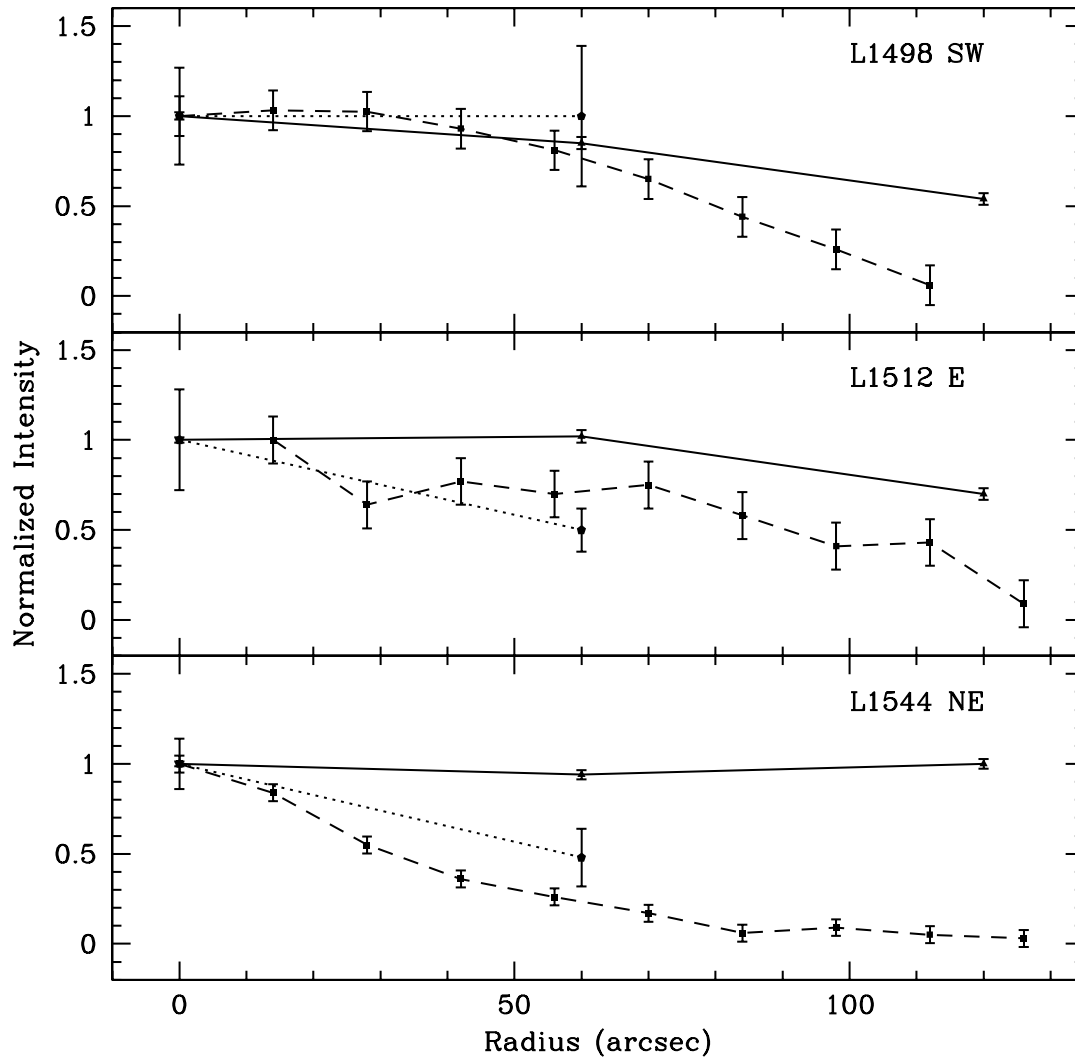


FIG. 7.— The solid lines are the normalized radial intensity profiles of the 6 cm H₂CO peak absorption (T_R). The dotted lines are profiles of the 1.3 mm H₂CO T_R . The dashed lines are the profiles of the 850 μ m dust emission. The slices are taken along the short axis of the PPCs as seen by the dust in the direction indicated in the figure. The error bars represent $\pm 1\sigma$; the largest error bar at 0'' is for the 1.3 mm data. The center positions are those given in the text for the H₂CO observations.

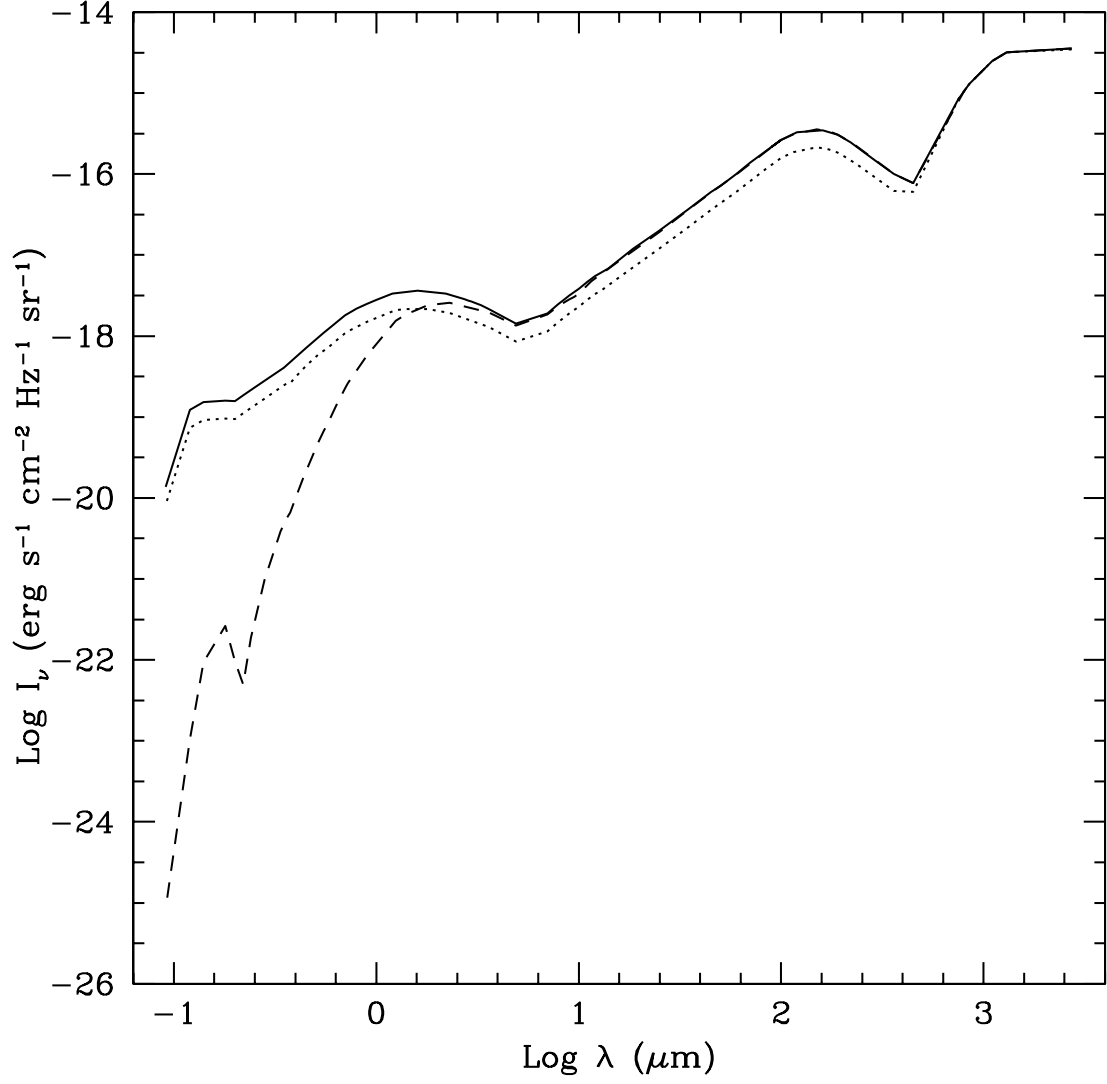


FIG. 8.— Plot of the standard ISRF (solid line), the reduced ISRF (dotted line), and the attenuated ISRF (dashed line). The reduced ISRF is weaker than the standard ISRF everywhere by a factor of 1.66. The attenuated ISRF ($A_V = 3$) is reduced from the standard ISRF predominately in the visible and UV.

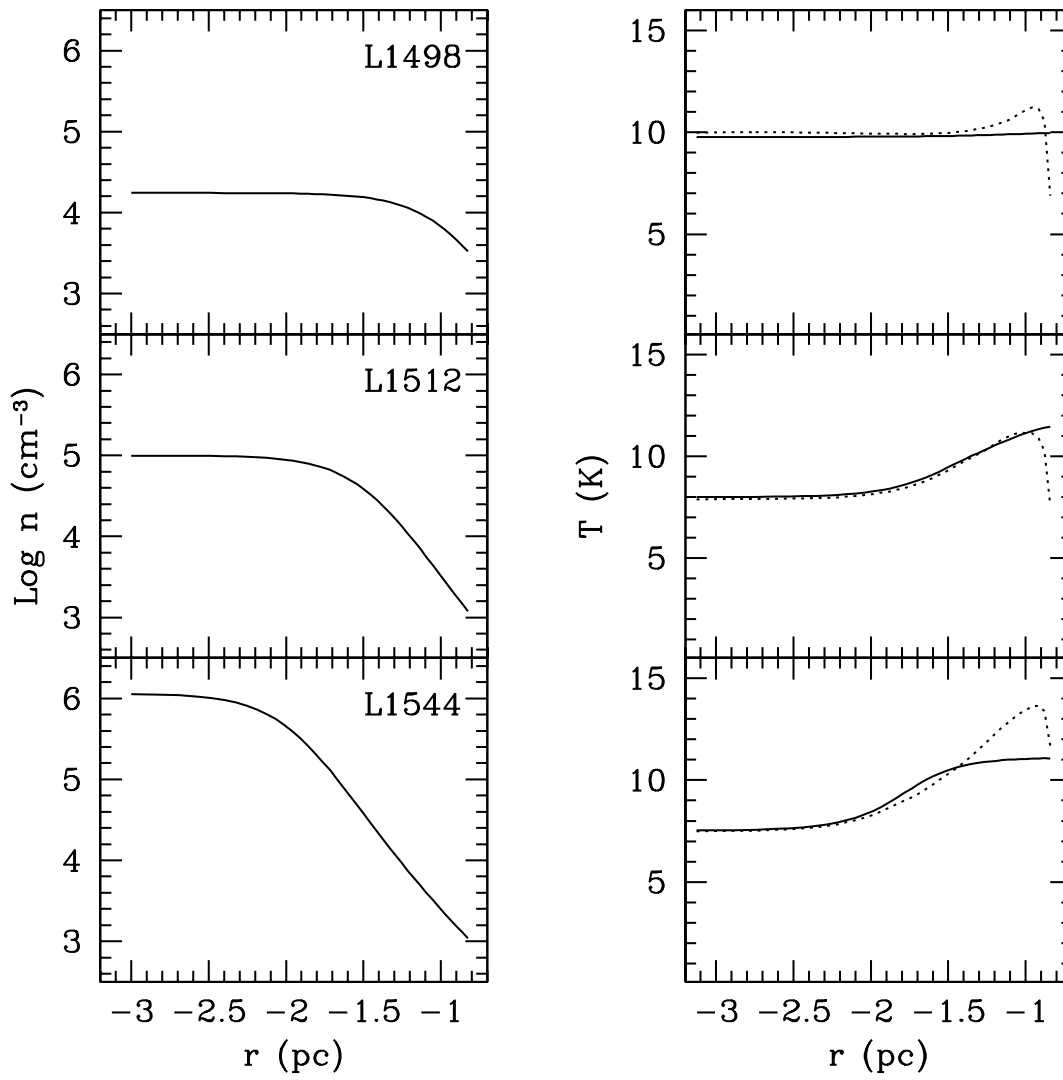


FIG. 9.— Model density and temperature versus radius for the three PPCs studied here. In the left column, the curve shows the density profile. In the right column, the solid line is the dust temperature and the dotted line is the gas temperature.

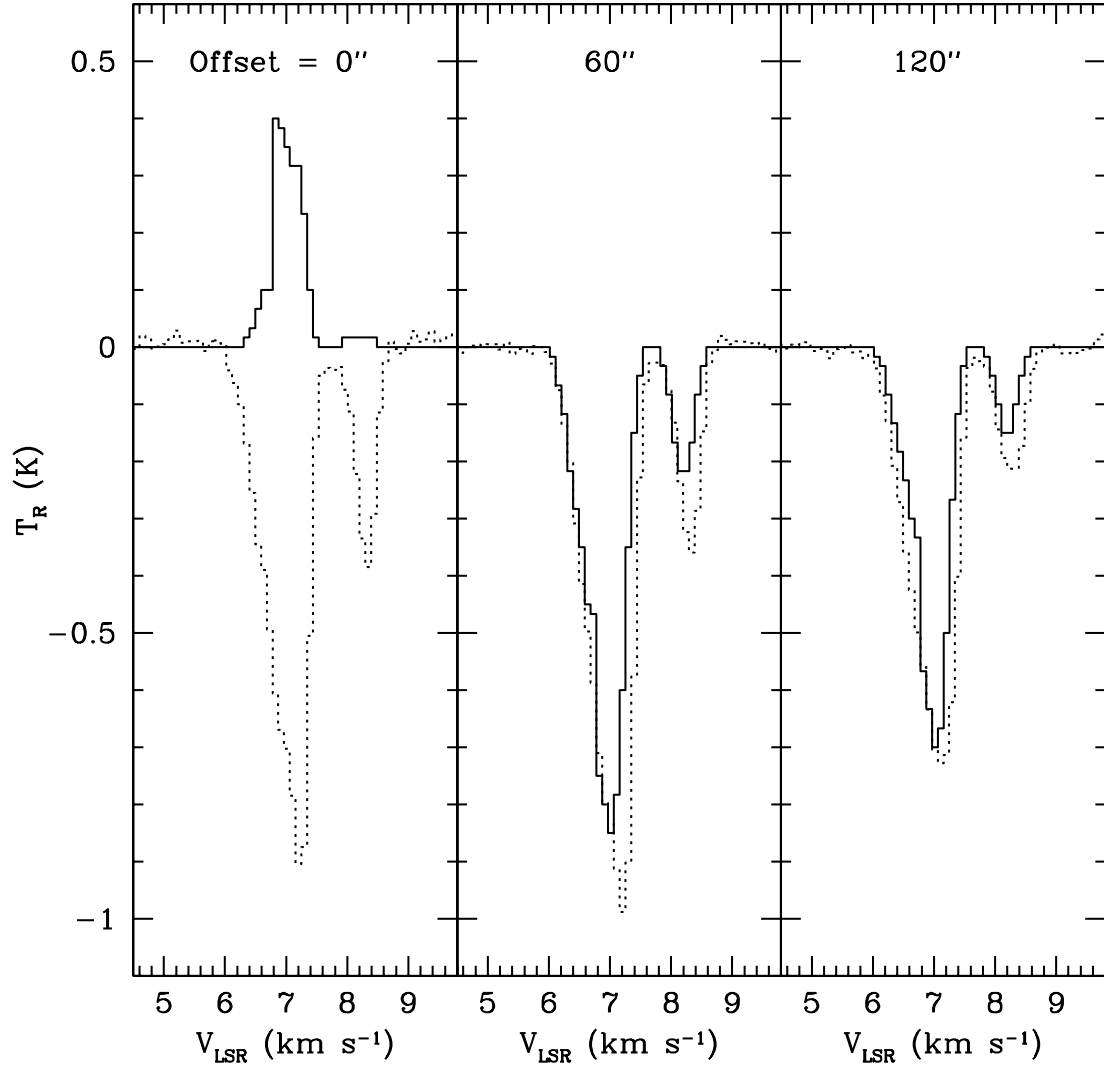


FIG. 10.— The solid line is a model of the expected H₂CO 6 cm line profile in a cold dense cloud with a central density of 10⁶ cm⁻³ and H₂CO abundance of 10⁻⁸. The dotted line is the observed spectrum of the 6 cm line in L1544. The figure illustrates that H₂CO must be depleted toward the center of the PPC.

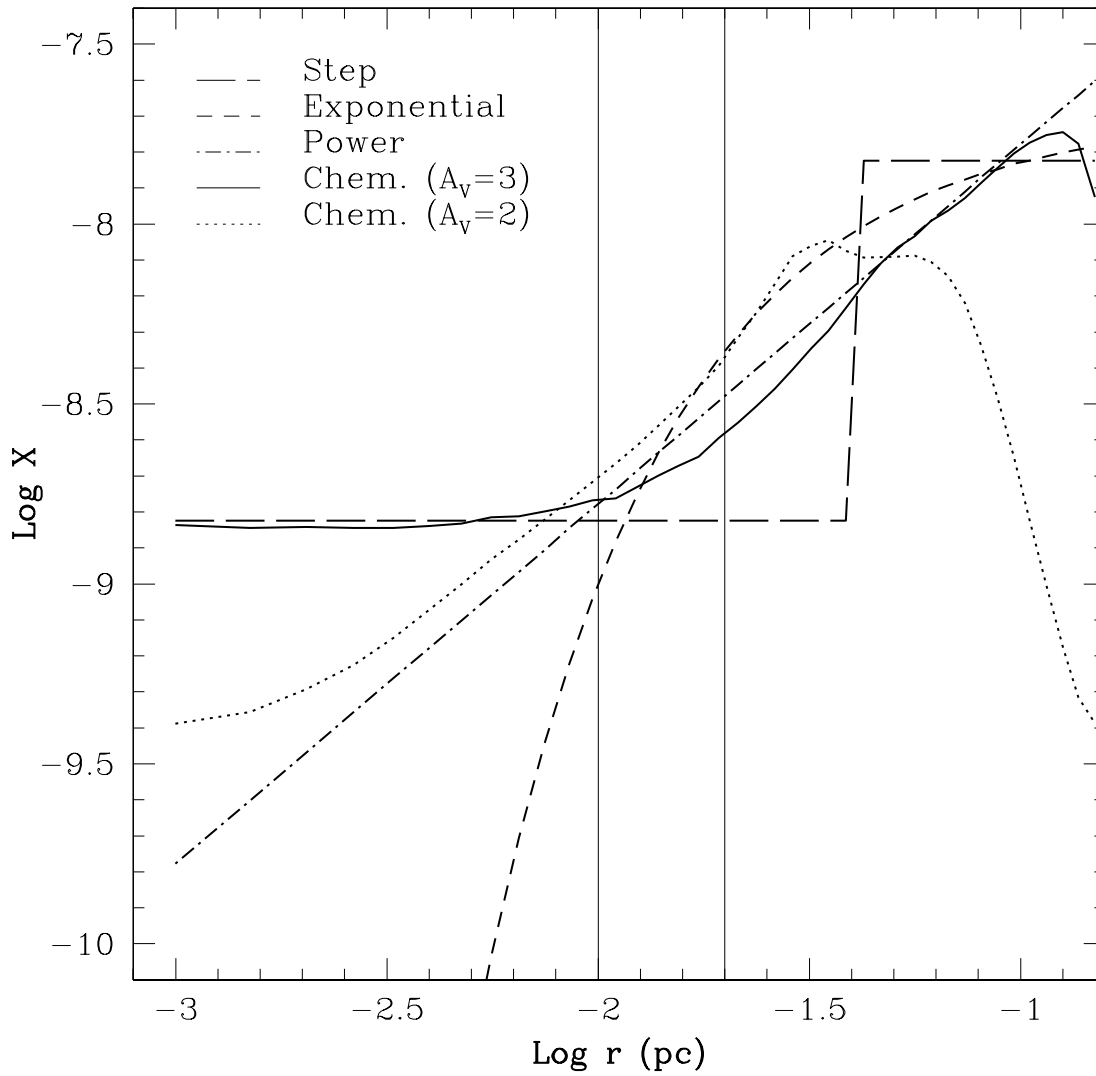


FIG. 11.— Examples of abundance profiles used in the models. The long dashed line is a step function. The short dashed line is an exponential. The dot-dash line is a power law. The solid line is the result of a chemical model with $A_V = 3$. The model parameters for these profiles are the same as for L1544 and are given in Table 3. The dotted line is the chemical model abundance profile for L1498 with $A_V = 2$. The amount of external extinction dramatically affects the chemical model abundance profile at large radii. The two vertical solid lines mark the radius of the beam for the 1.3 mm and 6 cm observations, $15''$ and $30''$, assuming a distance of 140 pc.

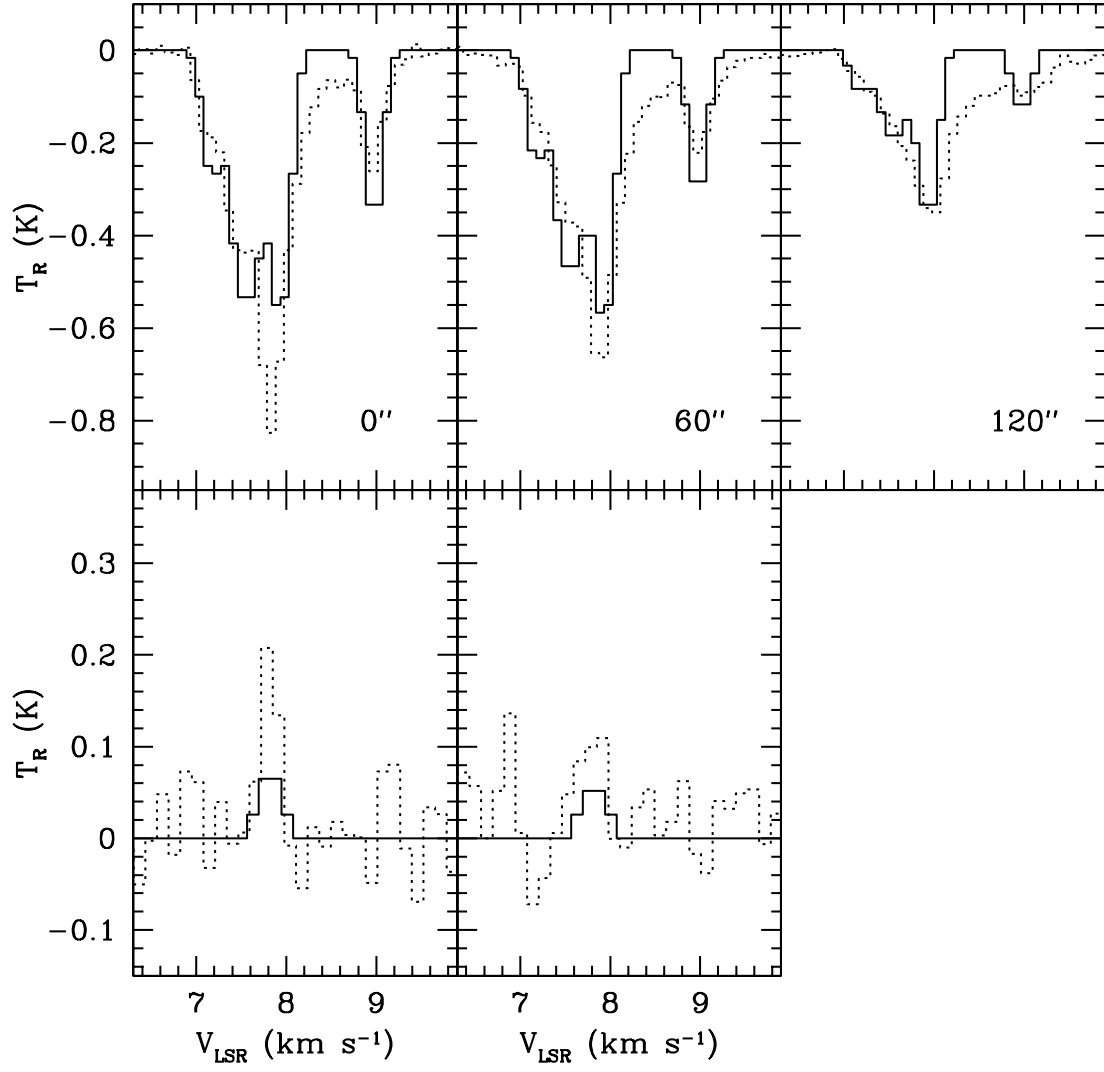


FIG. 12.— The dotted lines are the H $_2$ CO data, and the solid lines are the best-fit MC model for L1498. The top panels show the 6 cm line at the offsets indicated in the figure, and the bottom panels are the 1.3 mm line. The model has a chemical model abundance distribution. Model parameters are given in Table 3.

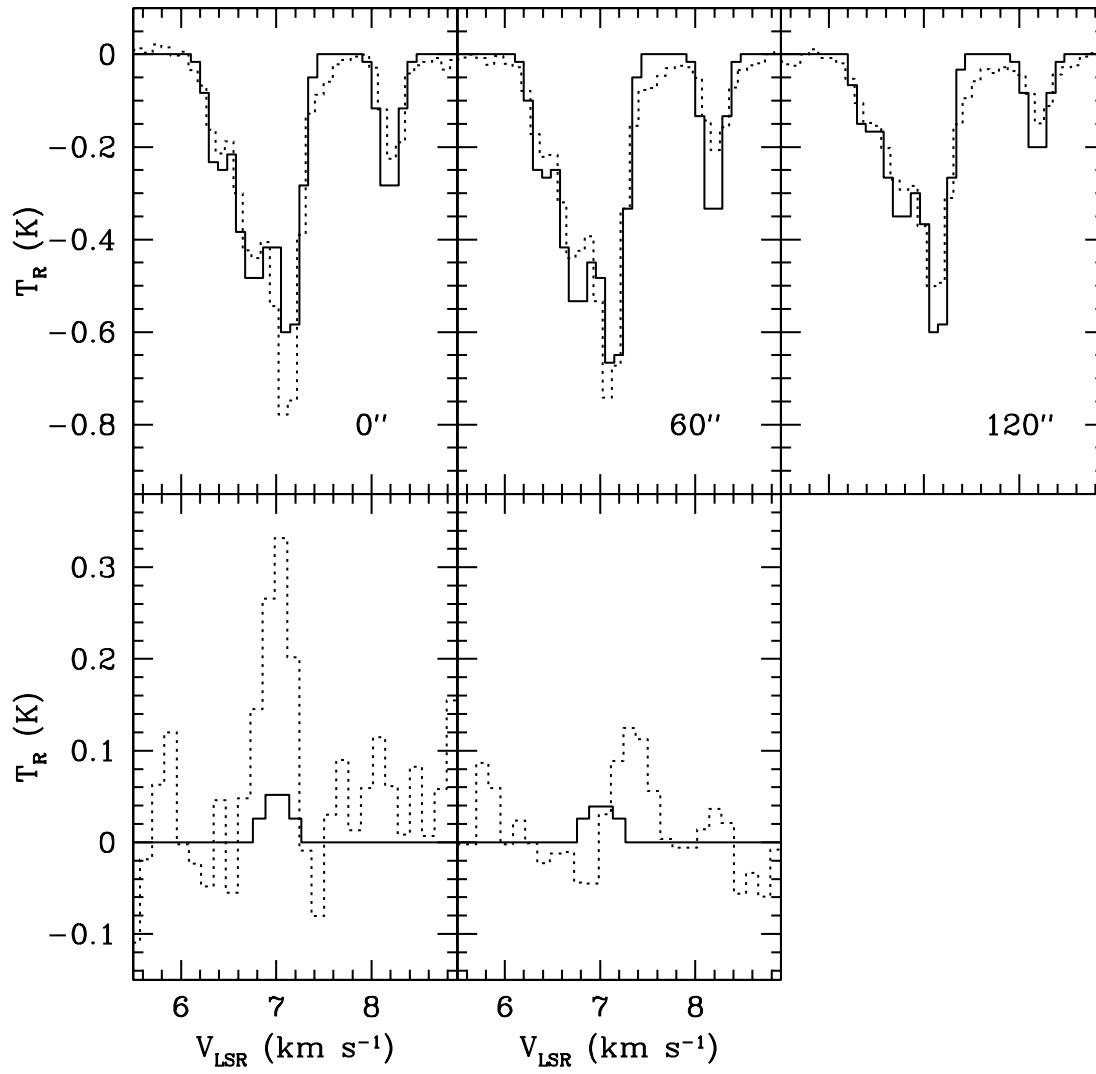


FIG. 13.— The dotted lines are the H_2CO data, and the solid lines are the best-fit MC model for L1512. The top panels show the 6 cm line at the offsets indicated in the figure, and the bottom panels are the 1.3 mm line. The model has a step function abundance distribution. Model parameters are given in Table 3.

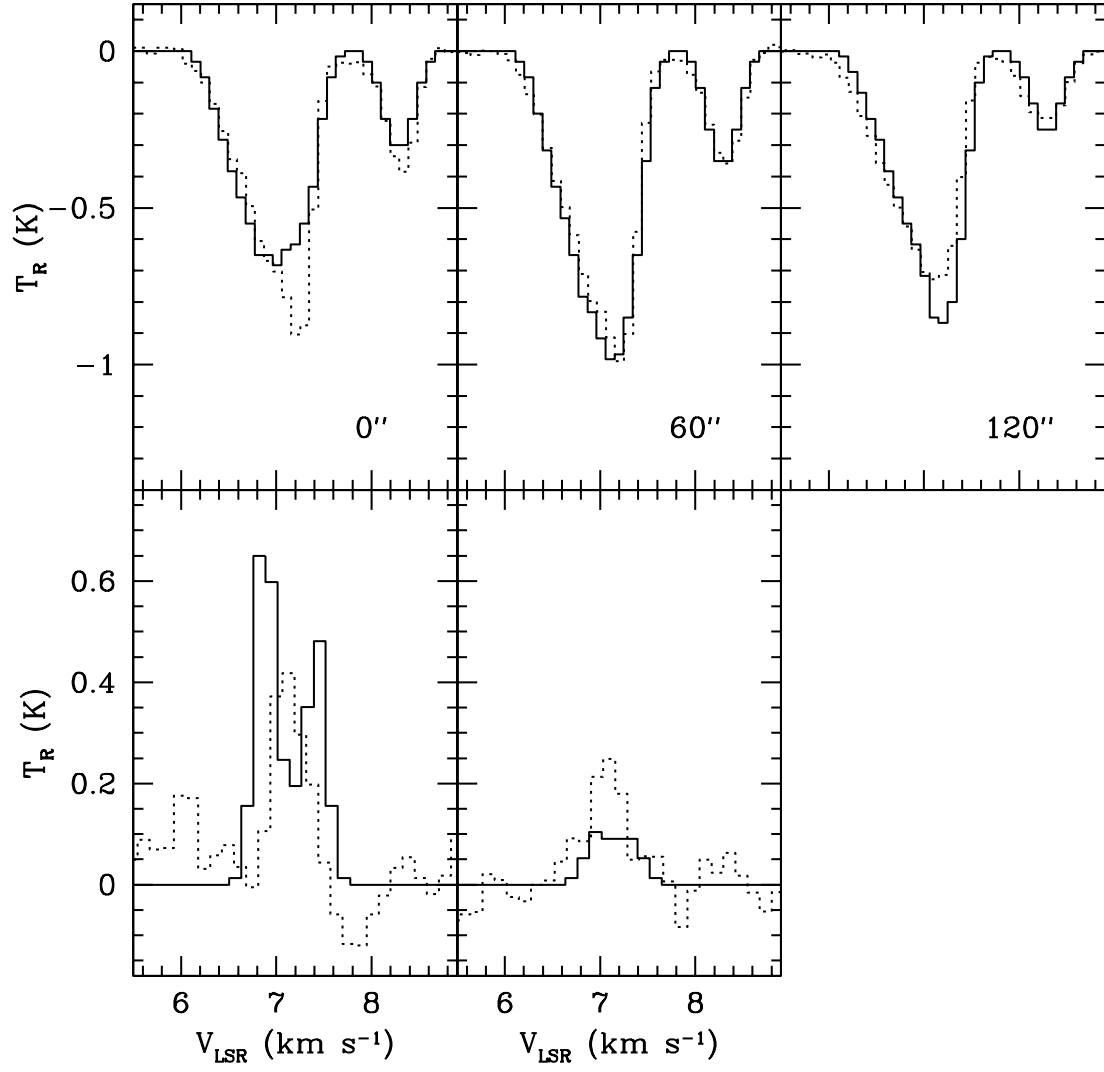


FIG. 14.— The dotted lines are the H_2CO data, and the solid lines are the best-fit MC model for L1544. The top panels show the 6 cm line at the offsets indicated in the figure, and the bottom panels are the 1.3 mm line. The model has a power law abundance distribution and a Plummer-like velocity profile. Model parameters are given in Table 3.

TABLE 1
H₂CO 6 CM LINE RESULTS

Source	Offset (', ')	v_{LSR} (km s ⁻¹)	Δv (km s ⁻¹)	σ_{turb} (km s ⁻¹)	T_R (K)	rms (K)	τ	T_{ex} (K)	N (10 ¹² cm ⁻²)	
L1498	(0,0)	7.85	0.35	0.14	-0.80	0.017	0.51	0.73	2.06	
	(0,0.7)	7.86	0.31	0.12	-0.78	0.025	0.75	1.24	4.27	
	(0,1.4)	8.02	0.72	0.30	-0.48	0.022	-	-	-	
	(0,-1.4)	7.94	0.37	0.15	-0.68	0.028	0.39	0.62	1.45	
	(0.7,0)	7.88	0.36	0.14	-0.73	0.023	0.69	1.26	4.62	
	(0.7,0.7)	7.97	0.64	0.27	-0.45	0.033	0.31	1.03	3.05	
	(0.7,2.1)	8.34	0.95	0.40	-0.18	0.020	-	-	-	
	(0.7,-0.7)	7.92	0.56	0.23	-0.75	0.030	-	-	-	
	(1.4,0)	7.98	0.60	0.25	-0.55	0.023	0.37	0.95	3.20	
	(1.4,1.4)	8.17	0.92	0.39	-0.30	0.032	-	-	-	
	(2.1,0.7)	8.16	0.80	0.34	-0.28	0.023	-	-	-	
	(-0.7,0.7)	7.85	0.28	0.11	-0.77	0.030	1.02	1.53	6.34	
	(-0.7,-0.7)	7.90	0.30	0.12	-0.68	0.025	1.31	1.66	7.43	
	(-0.7,-2.1)	8.03	0.37	0.15	-0.43	0.025	-	-	-	
	(-1.4,0)	7.89	0.28	0.11	-0.90	0.020	0.87	1.17	4.24	
	(-1.4,-1.4)	8.01	0.54	0.22	-0.43	0.028	0.53	1.68	6.97	
	(-2.1,-0.7)	7.92	0.34	0.13	-0.60	0.023	0.48	1.15	2.77	
L1512	(0,0)	7.11	0.26	0.10	-0.73	0.012	1.31	1.72	8.44	
	(0,1)	7.06	0.26	0.10	-0.65	0.025	1.30	1.83	8.89	
	(0,-1)	7.13	0.23	0.08	-0.77	0.032	1.23	1.64	6.71	
	(1,0)	7.11	0.26	0.10	-0.75	0.027	1.15	1.63	7.03	
	(1,1)	7.09	0.26	0.10	-0.80	0.025	0.99	1.45	5.49	
	(1,-1)	7.13	0.23	0.08	-0.65	0.023	1.45	1.88	8.99	
	(2,0)	7.15	0.30	0.12	-0.52	0.023	1.00	1.91	8.19	
	(2,1)	7.16	0.54	0.22	-0.38	0.022	-	-	-	
	(2,-1)	7.22	0.49	0.20	-0.22	0.018	-	-	-	
	(-1,0)	7.12	0.27	0.10	-0.80	0.025	1.17	1.56	7.17	
	(-1,1)	7.06	0.25	0.09	-0.75	0.018	1.48	1.75	9.37	
	(-1,-1)	7.12	0.25	0.09	-0.80	0.027	0.55	0.84	1.80	
	(-2,0)	7.12	0.28	0.11	-0.62	0.025	1.00	1.75	7.05	
	(-2,1)	7.06	0.25	0.09	-0.70	0.027	1.03	1.63	6.06	
	(-2,-1)	7.11	0.27	0.10	-0.55	0.027	0.64	1.56	3.92	
	L1544	(0,0)	7.21	0.31	0.12	-0.87	0.012	2.17	1.75	16.9
		(0,1.4)	7.14	0.38	0.15	-0.92	0.015	1.85	1.64	16.6
(0,-1.4)		7.27	0.28	0.11	-0.88	0.022	1.69	1.64	11.2	
(0.7,0.7)		7.14	0.43	0.17	-0.82	0.033	2.01	1.78	22.2	
(0.7,2.1)		7.03	0.35	0.14	-1.05	0.022	2.13	1.53	16.6	
(0.7,-0.7)		7.21	0.29	0.11	-1.05	0.022	2.00	1.51	12.8	
(1.4,0)		7.15	0.32	0.13	-1.12	0.017	1.53	1.30	9.35	
(1.4,1.4)		7.08	0.40	0.16	-0.87	0.027	2.16	1.74	21.7	
(2.1,0.7)		7.13	0.29	0.11	-1.25	0.022	1.68	1.19	8.58	
(-0.7,0.7)		7.23	0.33	0.13	-0.98	0.023	2.08	1.60	15.9	
(-0.7,-0.7)		7.25	0.27	0.10	-1.07	0.023	1.60	1.39	8.79	
(-0.7,-2.1)		7.27	0.30	0.12	-0.67	0.027	1.37	1.83	10.8	
(-1.4,0)		7.24	0.30	0.12	-1.10	0.027	2.03	1.46	13.0	
(-1.4,-1.4)		7.26	0.32	0.13	-0.68	0.027	1.37	1.81	11.3	
(-2.1,-0.7)		7.28	0.25	0.09	-0.63	0.017	1.49	1.91	10.1	

TABLE 2
H₂CO 1.3 MM LINE RESULTS

Source	Offset (', ')	v_{LSR} (km s ⁻¹)	Δv (km s ⁻¹)	σ_{turb} (km s ⁻¹)	T_R (K)	rms (K)	η_{MB}
L1498	(0,0)	7.82	0.23	0.08	0.23	0.043	0.53
	(0.7,0.7)	7.85	0.12	–	0.21	0.056	0.77
	(0.7,-0.7)	7.82	0.35	0.14	0.14	0.043	0.77
	(-0.7,0.7)	–	–	–	< 0.16 ^a	0.081	0.77
	(-0.7,-0.7)	7.85	0.25	0.09	0.23	0.056	0.77
L1512	(0,0)	7.01	0.35	0.14	0.34	0.079	0.53
	(0,1)	–	–	–	< 0.10 ^a	0.051	0.77
	(0,-1)	7.17	0.27	0.10	0.34	0.070	0.77
	(1,0)	7.09	0.31	0.12	0.17	0.029	0.77
	(-1,0)	7.12	0.13	0.02	0.18	0.034	0.77
L1544	(0,0)	7.14	0.41	0.17	0.47	0.063	0.57
	(0.7,0.7)	7.06	0.48	0.20	0.23	0.051	0.77
	(0.7,-0.7)	7.27	0.43	0.17	0.22	0.056	0.77
	(-0.7,0.7)	7.12	0.44	0.18	0.45	0.088	0.77
	(-0.7,-0.7)	–	–	–	< 0.12 ^a	0.058	0.77

^a2- σ upper limit

TABLE 3
MODEL PARAMETERS

Source	Abun. Prof.	X_0	r_D (pc)	Other	Abs. Dev. (6 cm)		Abs. Dev. (1.3 mm)	
					Int. ^a	Prof. ^b	Int. ^a	Prof. ^b
L1498	step	4×10^{-9}	0.02	$f_D=10$	0.17	1.28	0.053	0.29
	power	7×10^{-9}	–	$p=1^c$	0.25	1.43	0.055	0.30
	exponential	5×10^{-9}	0.02	–	0.17	1.28	0.055	0.30
	chemical ^d	0.8 ^e	–	$A_V=2, n_c=10^7 \text{cm}^{-3f}$	0.19	1.24	0.037	0.25
	chemical	2.0 ^e	–	$A_V=2, n_c=10^4 \text{cm}^{-3f}, G_0=0.6$	0.26	1.27	0.058	0.30
L1512	step ^d	1×10^{-8}	0.05	$f_D=20$	0.037	0.96	0.10	0.71
	power	1.5×10^{-8}	–	$p=1^c$	0.081	1.04	0.078	0.65
	exponential	1.5×10^{-8}	0.05	–	0.079	1.24	0.050	0.60
	chemical	0.3 ^e	–	$A_V=3, n_c=10^6 \text{cm}^{-3f}$	0.13	0.92	0.078	0.67
L1544	step	1.5×10^{-8}	0.04	$f_D=10$	0.13	1.07	0.15	0.97
	power	2.5×10^{-8}	–	$p=1^c$	0.09	0.91	0.21	1.12
	pow. + vel. ^d	2.5×10^{-8}	–	$p=1$, Plummer vel.	0.084	0.91	0.23	1.17
	exponential	2×10^{-8}	0.03	–	0.11	0.99	0.20	1.13
	chemical	0.5 ^e	–	$A_V=3, n_c=10^6 \text{cm}^{-3f}$	0.11	0.89	0.20	1.10

^aAverage absolute deviation of the integrated intensity of the model versus the observed lines over all offsets.

^bAverage absolute deviation of the modeled profile shape versus the observed profiles over all offsets.

^cPower law exponent.

^dBest-fit model described in text and shown in Figures 12 – 14.

^eSince the chemical models are not characterized by X_0 , this value indicates the scale factor for the chemical model abundance profile.

^fThese values for A_V and n_c describe the input for the chemical model and are independent of dust radiative transfer model values.

APPENDIX

APPENDIX: ENERGETICS

The gas temperature at each depth in the model is determined by balancing the local heating and cooling rates (Figure A15). The approach used is patterned after that of Doty & Neufeld (1997), but with updates that we describe here.

Before discussing the detailed heating and cooling rates, we note that all references to $n(\text{H}_2)$ correspond to H_2 number density. However, many of the adopted rates require the baryon number density, $n(\text{H}) \sim 2n(\text{H}_2) + 4n(\text{He})$ (assuming that there is only neutral and molecular gas, and low abundances of heavier elements). For a molecular gas with 25% helium by mass, $n(\text{He}) = 0.166n(\text{H}_2)$, and $n(\text{H}) = 2.66n(\text{H}_2)$. All expressions below have accounted for this fact.

The gas close to the surface is primarily heated by photoelectric heating. We follow the prescription of Bakes & Tielens (1994), namely

$$\Gamma_{\text{pe}} = 10^{-24} \epsilon G(r) n(\text{H}) \text{ ergs cm}^{-3} \text{ s}^{-1}, \quad (\text{A1})$$

where the efficiency, ϵ is given by

$$\epsilon = \frac{4.87 \times 10^{-2}}{1 + 4 \times 10^{-3} (G(r) T_K^{0.5} / n_e)^{0.73}} + \frac{3.65 \times 10^{-2} (T_K / 10^4)^{0.7}}{1 + 2 \times 10^{-4} (G(r) T_K^{0.5} / n_e)}. \quad (\text{A2})$$

In this expression, T_K is the temperature, n_e is the electron number density, and $G(r) = \bar{J}(r; E > 6\text{eV}) / \bar{J}(\text{ISRF}; E > 6\text{eV})$ is the ratio of the mean intensity of the local radiation field within the cloud to the mean intensity of the ISRF for energies above 6 eV – the energies above which photons can cause significant photoelectric heating (e.g., Juvela, Padoan, & Jimenez 2003). The electron number density is taken from chemical models similar to Doty et al. (2002), which include UV processing and attenuation. In the clouds we study, the product $G(r) T_K^{0.5} / n_e$ is small enough that the total heating rate scales with $G(r)$ and is nearly independent of the exact value of the electron number density.

The depth-dependent radiation field is determined by a self-consistent solution to the radiative transfer problem using the code of Egan, Leung, & Spagna (1988). In this case, we assume spherical symmetry, include scattering, and adopt the dust properties for coagulated grains with icy mantles described by Ossenkopf & Henning (1994; column (5) of Table 1). These assumptions are identical to those adopted for the dust radiative transfer models, providing a consistent approach. While the radiation field is a complicated function of depth, it is interesting to note that it is generally much stronger than would be calculated by taking a simple attenuation law used for plane-parallel slabs such as $G(r) = G_0 \exp(-a\tau_V)$, where τ_V is the extinction at V and a is commonly taken to be in the range of 1.8 (e.g., Tielens, private communication) to 2.5 (Hollenbach, Werner, & Salpeter 1971). In a spherical geometry, any point in space has a lower optical depth to the outside for non-normal rays than for the equivalent ray in a slab geometry. As a result, the radiation field along non-normal rays can penetrate further into spherical sources, leading to a higher radiation field (e.g., Flannery et al. 1980). In the models described in the text, the value of G_0 is varied until agreement with the CO $J = 1 - 0$ line is reproduced. Physically, this has the effect of accounting for variations in the incident radiation field due to local sources and/or attenuation by the surrounding low-density cloud.

Grain photoelectric heating usually dominates in the exterior of the cloud. However, due to attenuation of the photon flux by the dust, cosmic ray heating will often dominate in the interior ($\tau_V > 1$), as can be seen in Figure A15. We assume a cosmic-ray ionization rate of $3 \times 10^{-17} \text{ s}^{-1}$ (van der Tak & van Dishoeck 2000), and also take the energy input per ionization to be $\Delta Q = 20 \text{ eV}$ (Goldsmith 2001). This yields a cosmic ray heating rate per unit volume of

$$\Gamma_{\text{gas,cr}} = 10^{-27} n(\text{H}_2) \left[\frac{\zeta}{3 \times 10^{-17} \text{ s}^{-1}} \right] \left[\frac{\Delta Q}{20 \text{ eV}} \right] \text{ ergs cm}^{-3} \text{ s}^{-1}. \quad (\text{A3})$$

For the gas cooling, we follow Doty & Neufeld (1997) in their adoption of the tabulated cooling functions of Neufeld, Lepp, & Melnick (1995) and Neufeld & Kaufman (1993) for CO, OI, H_2 , H_2O , and other diatomic and polyatomic molecules. As discussed in the text, molecular depletion is a key aspect of these clouds. However we have not decreased the abundances of coolants because the abundances are strongly affected only at relatively high densities, where T_K is already closely coupled to T_d . Depletion has only a small effect on gas temperature (Goldsmith 2001). Similar to Doty & Neufeld (1997), we find that the cooling in the exterior is dominated by CO. Likewise, the decrease in temperature on the outside of the models is due to the increased ability of radiation to escape, allowing the gas to cool. We tested the case where the gas temperature is constant at the outer radii rather than decreasing and found that the drop off in T_K at large radii causes a $\sim 5\%$ decrease in T_R .

Collisions between gas and dust can either heat or cool the gas; the dust will cool the gas if the gas kinetic temperature, T_K , is greater than the dust temperature, T_d , and vice-versa. Our formulation treats the interaction as a cooling term formally. There is of course a balancing heating or cooling of the dust in the process, but the effect on T_d is small compared to radiative processes, even deep in well-shielded clouds (Evans et al. 2001, Goldsmith 2001), and we ignore it here. We adopt the general prescription of Hollenbach & McKee (1989), assuming collisions between gas and dust where the dust has a power-law size distribution $n(a) \propto a^{-3.5}$ (Mathis, Rumpl, & Nordsieck 1977), with a minimum grain size $a_{\text{min}} = 100 \text{ Angstroms}$, a maximum grain size $a_{\text{max}} = 0.25 \mu\text{m}$, a mass density $\rho = 2 \text{ g cm}^{-3}$, and a dust-to-gas mass ratio of $R_{\text{dg}} = 4.86 \times 10^{-3}$. These assumptions lead to an average dust cross section per baryon of $\Sigma_d = 6.09 \times 10^{-22} \text{ cm}^{-2}$. We adopt the temperature-dependent accommodation coefficient

$\alpha = 0.37[1 - 0.8\exp(-75/T_K)]$ (Burke & Hollenbach 1983). This expression comes from averaging over speeds for an astrophysical mixture of gases; thus it must be used in conjunction with a mean speed for a hydrogen atom, $\langle v(m_H) \rangle$. With these conventions, our adopted expression for the gas-dust energy transfer rate is

$$\Lambda_{\text{gd}} = 9.0 \times 10^{-34} n(\text{H})^2 (T_K)^{0.5} \left(1 - 0.8 \times \exp\left(-\frac{75}{T_K}\right) \right) (T_K - T_d) \left[\frac{\Sigma_d}{6.09 \times 10^{-22}} \right] \text{ ergs cm}^{-3} \text{ s}^{-1}. \quad (\text{A4})$$

This expression is similar in form to others in the literature. However, the coefficient is approximately the geometrical mean of the lower value of Goldsmith (2001) and the higher value of Hollenbach & McKee (1989). It is, however, within a factor of 5 of these two other values. This is reassuring as our expression does not represent an extremum on either end of the range of expected gas-dust cooling rates, and agrees to within the intrinsic uncertainties in assumed microphysical properties (e.g., dust composition, size distribution, dust-gas mass ratio, sticking probabilities, gas composition, etc.). In practice, gas-dust cooling has the effect, as noted by other authors (e.g., Doty & Neufeld 1997; Goldsmith 2001), of strongly coupling the gas and dust temperatures at densities $n > 10^5 \text{ cm}^{-3}$.

These heating and cooling rates are then solved for the temperature point-by-point within the cloud. The problem is treated as a root-finding problem in the gas temperature, and solved using Brent's method (Press et al. 1992) to a fractional accuracy of 10^{-8} .

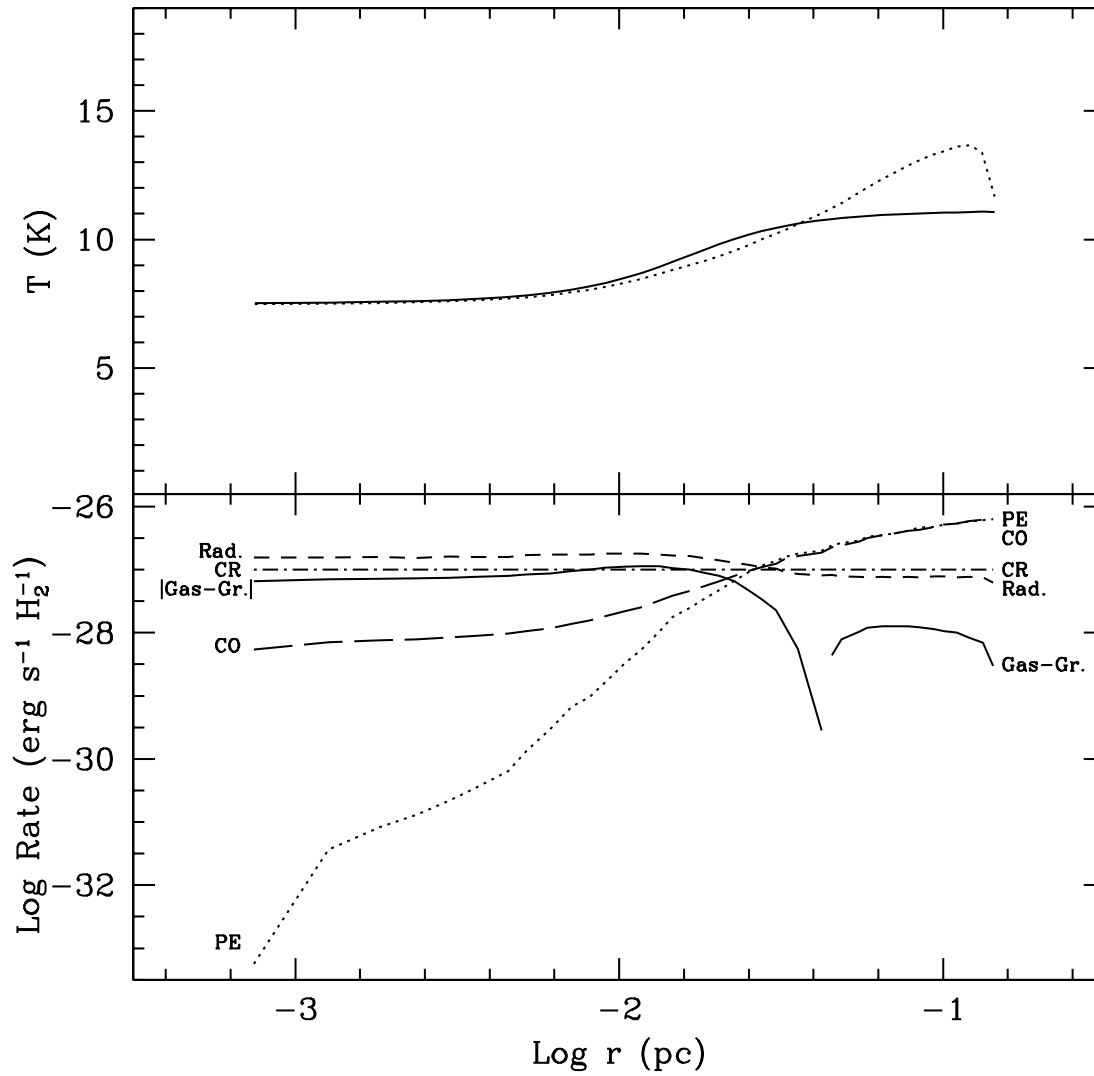


FIG. A15.— The top panel shows the dust temperature (solid line) from the dust radiative transfer model and the gas temperature (dotted line) produced by the energetics code for a model of L1544. The bottom panel shows the heating and cooling rates per hydrogen molecule in the energetics code. The lines represent, from top to bottom on the left side, the total gas radiative cooling, cosmic ray heating, the absolute value of the gas-grain energy exchange, CO radiative cooling, and the photoelectric effect. The break in the solid line represents the point at which the gas-grain energy transfer is no longer heating the gas. At high density and low temperature, in the inner parts of the PPC, the total gas radiative cooling is large compared to CO cooling due mainly to the contributions of isotopologues of CO.